Hindawi
International Journal of Energy Research
Volume 2023, Article ID 9881400, 23 pages
https://doi.org/10.1155/2023/9881400

Research Article

Integration of Highly Graphitic Three-Dimensionally Ordered Macroporous Carbon Microspheres with Hollow Metal Oxide Nanospheres for Ultrafast and Durable Lithium-Ion Storage

Soo Young Yang[1], **Jin-Sung Park**[1], **Hye Young Koo**[2], **and Yun Chan Kang**[1]

[1]*Department of Materials Science and Engineering, Korea University, Anam-Dong, Seongbuk-Gu, Seoul 136-713, Republic of Korea*
[2]*Department of Metal Powder, Korea Institute of Materials Science, 797 Changwon-daero, Changwon, Gyeongnam 51508, Republic of Korea*

Correspondence should be addressed to Hye Young Koo; hykoo@kims.re.kr and Yun Chan Kang; yckang@korea.ac.kr

Received 25 April 2023; Revised 12 August 2023; Accepted 8 November 2023; Published 1 December 2023

Academic Editor: Abdulkerim Okbaz

Achieving excellent electrochemical performance at high charging rate has been a long-cherished dream in the field of lithium-ion batteries (LIBs). As a part of the efforts to meet the goal, an innovative strategy for the synthesis of 3D porous highly graphitic carbon microspheres, to which numerous hollow metal oxide nanospheres are anchored, for use as anode in LIBs is introduced. Hollow carbon nanosphere-aggregated microspheres prepared from the spray drying process are graphitized with the aid of metal catalysts, and subsequent oxidation selectively removed amorphous carbon, leading to the formation of highly conductive graphitic carbon matrix. Numerous hollow metal oxide nanospheres formed simultaneously during the oxidation process via nanoscale Kirkendall diffusion are anchored onto the carbonaceous matrix, effectively reinforcing the structural integrity by alleviating volume changes and reducing lithium-ion diffusion lengths. The synergistic effect of combining hollow metal oxide nanospheres with high theoretical capacity with conductive carbon matrix led to accelerated electrochemical kinetics, resulting in high capacity at high charging rate. In addition, trapping the hollow metal oxide nanospheres inside hollow carbon nanospheres could effectively alleviate the volume changes, which led to high structural stability. When applied as LIB anodes, the microspheres exhibit a capacity of 411 mA h g^{-1} after 2500 cycles at 10.0 A g^{-1}, with ~80% capacity retention. The anode exhibits a high capacity of 274 mA h g^{-1} at an extremely high current density of 50.0 A g^{-1}, thus demonstrating the structural merits of the microspheres.

1. Introduction

Achieving satisfactory capacity and stable cycle performance at high charging rates are the fundamental objectives for lithium-ion batteries (LIBs) [1, 2]. Accordingly, incessant efforts have been devoted to the development of anode materials with superb electrochemical properties [3–5]. Among the various materials of choice, transition metal compounds have been extensively investigated because of their high theoretical capacities when applied as anodes in LIBs [6–11]. Unfortunately, they suffer from capacity decay due to the strain arising from repetitive volume changes and poor rate capability due to low electrical conductivity [12–15]. To overcome these drawbacks, the design and synthesis of nanostructured anode materials are considered as a highly effective strategy for prolonging the cycle life and enhancing the rate capability [16, 17]. Chen et. al developed various materials with numerous compositions, which can be applied for enhancing the electrochemical performance [18–24]. The introduction of pores within the nanostructured anode material can improve the structural robustness due to the alleviation of volume changes during repetitive cycling and enhance the rate capability owing to the facile penetration of electrolyte and reduced lithium-ion diffusion path [25, 26]. The nanoscale Kirkendall effect can be an efficient method for the preparation of hollow nanoparticles

since they do not require additional template-removal steps [27, 28]. Cho et al. prepared nanofibers comprising hollow NiO nanospheres by applying an electrospinning process together with the Kirkendall effect [29]. The anode exhibited a stable cycle performance, wherein a capacity of 707 mA h g^{-1} was observed after 250 cycles at 1.0 A g^{-1}, and satisfactory rate capability (636 mA h g^{-1} at 3.0 A g^{-1}) was also achieved.

Another effective strategy to enhance the battery performance is compositing with carbonaceous materials, which would allow to reduce the strain imposed on the active material during volume changes and also endow supplementary electrical conductivity [30, 31]. Many efforts have been put into compositing metal oxide materials with carbon [32–34]. Song et al. prepared porous carbon-assisted CNT-supporting Fe_3O_4 nanoparticles, which enabled stable cycle performance up to 700 cycles at 1 A g^{-1} [35]. In addition, Gu et al. prepared graphene nanosheet-loaded Fe_3O_4 nanoparticles, which exhibited stable cycle life and good rate capability [36]. Graphitic carbon, which generally exhibits higher electrical conductivity than amorphous carbon, has been composited with transition metal compounds to improve structural robustness and electrochemical kinetics [37–39]. For example, Wang et al. prepared coral-like FeP composited with graphitic carbon, which exhibited a stable cycle performance (297 mA h g^{-1} after 1000 cycles at 1.0 A g^{-1}) and high rate capability (238 mA h g^{-1} at 20.0 A g^{-1}) [40]. Various three-dimensional (3D) porous amorphous carbon matrices, to which transition metal compounds are anchored, have been reported to act as efficient electron transport pathways [41–43]. It would be highly desirable if the 3D carbon matrix could be graphitized, which enables higher electrochemical kinetics. Amorphous carbon is generally known to be graphitized at extremely high temperatures under inert atmosphere, but the temperature can be significantly reduced to below 1000°C in the presence of a metal with catalytic effect [44, 45].

In this study, 3D porous and highly graphitic carbon microspheres, to which numerous hollow metal oxide nanospheres are anchored (denoted as G-HCA-Fe_2O_3, where G-HCA refers to graphitic hollow carbon aggregate), are synthesized via spray drying, graphitization in the presence of nanosized metal catalysts, and applying the nanoscale Kirkendall effect. Iron oxide is selected as the first target material; iron nitrate is infiltrated into the abundant pores of the 3D porous carbon microspheres obtained through spray drying. Subsequent heat treatment of the composite powder in an Ar atmosphere results in the formation of Fe metal nanoparticles, which trigger the in situ graphitization of carbon. Then, the resultant powder was oxidized at 350°C, which resulted in the formation of G-HCA-Fe_2O_3 microspheres. The specific temperature (350°C) can selectively eliminate amorphous carbon given that graphitic carbon with a highly ordered structure can withstand relatively high temperatures. During oxidation, dense Fe nanospheres are transformed into their hollow Fe_2O_3 counterparts owing to the nanoscale Kirkendall effect. The formation mechanism is comprehensively investigated by examining the structural evolution using various analyses at each step. When applied as an anode for LIBs, G-HCA-Fe_2O_3 microspheres exhibit a stable cycle performance for 2500 cycles at 10.0 A g^{-1} and a high capacity even at an ultrahigh current density of 50.0 A g^{-1}. Due to the structural merits where hollow Fe_2O_3 nanospheres with short lithium diffusion length are well dispersed in the conductive 3D porous graphitic carbon microspheres, anodes with structural robustness at fast charging speeds could be realized.

2. Experiment

2.1. Sample Preparation

2.1.1. Preparation of Hollow Carbon Aggregate Microspheres. Hollow carbon-aggregated (HCA) microspheres were prepared from spray drying of aqueous solution containing dextrin and colloidal SiO_2@resorcinol-formaldehyde (RF) core–shell nanospheres. Colloidal SiO_2@RF nanospheres were prepared as follows: ammonia solution (7 mL, SAMCHUN, 25.0%) was added to a 160 mL solution comprising distilled water (20 mL) and ethanol (140 mL), which was stirred vigorously for 5 min. Tetraethyl orthosilicate (7 mL, SAMCHUN, 95.0%) was added to the solution and stirred for an additional 15 min. Further addition of resorcinol (0.8 g, SAMCHUN, 98.0%) and formaldehyde (1.12 mL, Junsei, 36.0%) and stirring overnight at a temperature of 70°C resulted in the formation of RF shell. Spray drying was applied to synthesize HCA microspheres as follows: the colloidal solution containing SiO_2@RF core–shell nanospheres was centrifuged once and then redispersed in distilled water, and dextrin (5 g L^{-1}, SAMCHUN, 99.5%) was added. A two-fluid nozzle was used to atomize the aqueous solution at a pressure of 2.0 bar, and the inlet and outlet temperatures were set to 300 and 120°C, respectively. To carbonize the obtained powder, it was heat-treated at 700°C for 5 h under a flow of Ar gas inside a quartz tube. Finally, the powder was dipped in an aqueous NaOH solution to etch SiO_2, yielding HCA microspheres.

2.1.2. Preparation of G-HCA-Fe_2O_3 Microspheres. G-HCA-Fe_2O_3 microspheres were prepared via a salt-impregnation technique using a drop-and-dry process. Ethanol solution containing iron nitrate (0.05 g, SAMCHUN, 98.5%) was added dropwise to HCA powder (0.02 g) and then mixed in a mortar. The iron nitrate-infiltrated HCA microspheres were placed in an alumina boat and heated at 900°C at a ramping rate of 5°C min^{-1} for 3 h under an Ar gas flow, thus forming GA-HCA-Fe microspheres. The resultant powder was subsequently heat-treated at 350°C (ramping speed: 5°C min^{-1}) for 3 and 12 h under an air atmosphere to form GA-HCA-Fe_2O_3 and G-HCA-Fe_2O_3, respectively.

2.1.3. Preparation of Carbon-Free Fe_2O_3 Microspheres. Carbon-free Fe_2O_3 microspheres were prepared to understand the roles of HCA microspheres on the electrochemical properties. Iron nitrate-infiltrated HCA microspheres (0.05 g:0.02 g) were placed in an alumina boat and heated at 350°C with a ramping rate of 5°C min^{-1} for 12 h in air.

2.2. Material Characterization. Field-emission scanning electron microscopy (FE-SEM; Hitachi, S-4800) and transmission electron microscopy (FE-TEM; JEOL, JM-2100F) were used to investigate the morphology of the prepared microspheres. The crystallographic features of the samples were investigated using X-ray diffraction (XRD; PANalytical, X'Pert PRO with Cu $_{\alpha}$ radiation) at the Korea Basic Science Institute (KBSI, Daegu). The chemical nature of the samples was characterized using X-ray photoelectron spectroscopy (XPS; Thermo Scientific K-Alpha™) with focused monochromatic Al K_{α} radiation. The carbon structure was analyzed using Raman spectroscopy (Jobin Yvon LabRam HR800) with a 632.8 nm He/Ne laser as the excitation source. Thermogravimetric analysis (TGA, Pyris 1 Thermogravimetric Analyzer, Perkin Elmer) was conducted in the temperature range of 25–800°C at a ramping speed of $10^{\circ}C\,min^{-1}$ in the air to determine the amount of carbon in the samples. The pore structures and specific surface areas of the samples were analyzed using the Brunauer-Emmett-Teller method with nitrogen gas as the adsorbate.

2.3. Electrochemical Measurements. Electrochemical measurements were performed using 2032-type coin cells assembled in a glove box. To prepare the electrode, the active material:carbon black (Super P):sodium carboxymethyl cellulose binder in a weight ratio of 7 : 2 : 1 was mixed in the presence of distilled water in a mortar. The prepared slurry was cast onto a copper foil using a doctor's blade. The electrode was punched in a circle with a diameter of 1.4 cm and an average loading mass of $1.2\,mg\,cm^{-2}$. Lithium metal and microporous polypropylene films were used as the counter electrode and separator, respectively. $LiPF_6$ (1 M) in fluoroethylene carbonate and dimethyl carbonate (1 : 1 *v*/*v*) was used as the electrolyte. The coin cells were galvanostatically charged and discharged in the potential range of 0.001-3.0 V at various current densities to analyze their electrochemical properties. Cyclic voltammograms of the electrode materials were obtained in the same potential range at scan rates varying from 0.1 to $2.0\,mV\,s^{-1}$ to clarify the electrochemical reactions and kinetics. Electrochemical impedance spectroscopy (EIS) was performed in situ and ex situ at frequencies ranging from 0.01 Hz to 100 kHz.

3. Results and Discussion

A schematic of the formation of G-HCA-Fe_2O_3 microspheres prepared via spray drying and two-step heat treatment is shown in Scheme 1. Initially, a 3D porous microspherical carbonaceous matrix (referred to as hollow carbon aggregated (HCA) microspheres) was prepared through facile spray drying of an aqueous solution in which SiO_2@resorcinol-formaldehyde (RF) nanospheres are dispersed. Following the method used in previous studies, SiO_2@RF nanospheres were synthesized in an ethanol/water medium, which was centrifuged and redispersed in distilled water [46]. Spray drying the brownish colloidal solution in which dextrin was dissolved resulted in the clustering of nanometer-sized SiO_2@RF spheres into microspheres with an average size of 2.68 μm. Here, dextrin played an important role in tightly integrating the particles together. Microspheres consisting of numerous SiO_2@C nanospheres were obtained via heat treatment under an Ar atmosphere, which carbonized the RF polymer shell; SiO_2 cores were subsequently removed by immersion in NaOH solution. SiO_2 was also present in the carbon shell, and its removal enabled the formation of ample pores. An ethanol solution containing iron nitrate salt was dropped and dried repeatedly to HCA powder, which triggered the infiltration of metal salt into the pores due to the capillary force. Heat treatment of the iron nitrate-containing HCA microspheres under Ar atmosphere at 900°C led to the graphitization of carbon owing to the catalytic effect of metallic Fe nanoparticles, resulting in the formation of GA-HCA-Fe microspheres (GA-HCA refers to HCA microspheres consisted of both graphitic and amorphous carbon) [45]. Role of transition metal catalysts in the graphitization of carbon was discussed in the previous studies [47, 48]. Two main types of mechanisms include (1) the dissolution of carbon into molten metal and the precipitation of metal and graphite crystals from saturation and (2) the formation of intermediate metal carbide, which is decomposed and recrystallized to metal and graphite crystals. The crystal growth of Fe nanoparticles was inhibited because iron nitrate was located inside the pores of the shells of HCA microspheres. Owing to the Ostwald ripening process, Fe metal nanoparticles migrated outside the carbon shell and thus formed onion-like graphitic carbon rings in the shells of the hollow carbon nanospheres [49]. Subsequent oxidation of the powder at 350°C for 3 h selectively removed some of the amorphous carbon, and hollow Fe_2O_3 nanoparticles were formed owing to the nanoscale Kirkendall effect, leading to the formation of GA-HCA-Fe_2O_3 microspheres. In the initial state of oxidation, a thin layer of Fe_2O_3 was formed on the surface of the Fe metal nanoparticles, thus forming an intermediate core–shell structure. Because iron cations with ionic radii of 76 and 65 pm for Fe^{2+} and Fe^{3+} oxidation states, respectively, diffused outward more rapidly than oxygen anions with radius of 140 pm diffused inward, void spaces were generated adjacent to the Fe–Fe_2O_3 interface. Increasing the oxidation time to 12 h removed most of the amorphous carbon, and microspheres comprised of highly graphitic hollow carbon nanospheres to which hollow Fe_2O_3 nanospheres are anchored on (G-HCA-Fe_2O_3 microspheres) could be synthesized.

Scanning electron microscopy (SEM) images of microspheres comprising SiO_2@RF nanoparticles prepared via spray drying are shown in Figure S1. Carbonization of the microsphere resulted in the formation of SiO_2@C microspheres (Figure S2), whose SiO_2 located at the core and shell of each carbon nanosphere was later removed by NaOH etching process. SEM images of HCA microspheres are shown in Figure S3a, and the hollow nature of each carbon nanosphere constituting the microsphere can be confirmed from the transmission electron microscopy (TEM) image (Figure S3b). To clarify the role of dextrin in forming a highly integrated 3D carbon matrix, HCA microspheres were prepared from a solution without dextrin and etched with a NaOH solution. Disintegration

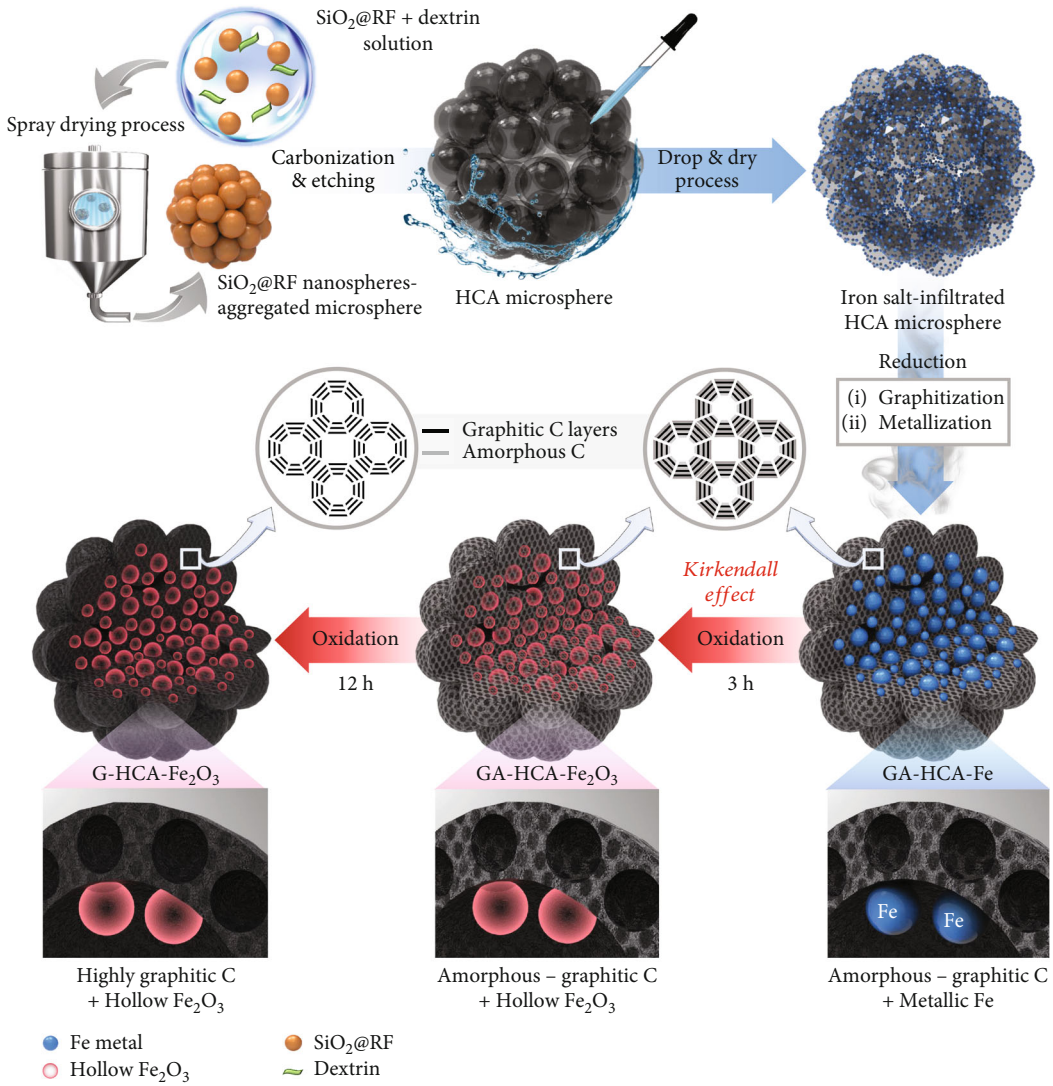

Scheme 1: Schematic illustration showing the formation mechanism of G-HCA-Fe_2O_3 microspheres.

of the particles was observed in the SEM image (Figure S4) after NaOH etching, which revealed that dextrin played the role of tightly binding the hollow carbon nanospheres together. The morphology of HCA microspheres is well maintained after the iron salt is infiltrated via the drop-and-dry process, as shown in Figure S5. The morphological traits, selected area electron diffraction (SAED) patterns, and elemental mapping images of GA-HCA-Fe microspheres obtained from the heat treatment of iron salt infiltrated HCA microspheres under Ar atmosphere were closely examined (Figure 1). The SEM image (Figure 1(a)) reveals the microspherical morphology with nonaggregation characteristics between the microspheres. The surface of the hollow carbon nanospheres constituting the microspheres appears to be more roughened than that of HCA microspheres (Figure S3), probably owing to the graphitization of carbon. The XRD pattern of GA-HCA-Fe microspheres (Figure S6) revealed that α-Fe and γ-Fe phases (JCPDS card #06-0696 and #23-0298, respectively) were formed after the heat treatment under an Ar atmosphere. According to a previous study, reduction of iron occurs upon the increase in temperature; iron compound then undergoes a carbothermic reduction to form an intermediate carbide (Fe_xC) [48]. When the temperature was increased further, the carbide decomposes, and only metallic Fe could be observed. Notably, peaks corresponding to graphitic carbon (#75-2078) are observed, which confirms that amorphous carbon is graphitized owing to the catalytic effect of Fe metal during the heat treatment. This is further evidenced by the fact that peaks corresponding to graphitic carbon are not observed for HCA microspheres heat-treated under an Ar atmosphere (Figure S7). Small Fe particles are uniformly distributed over the microspheres, as shown in the TEM image in Figure 1(b). Since Fe nanoparticles appear relatively darker in comparison to carbon materials, it can be observed that they are anchored onto hollow graphitic carbon nanospheres (Figure 1(c)). Fe nanoparticles with small sizes were observed even after heat treatment at 900°C, since iron nitrate was originally located inside the pores of the hollow carbon nanospheres

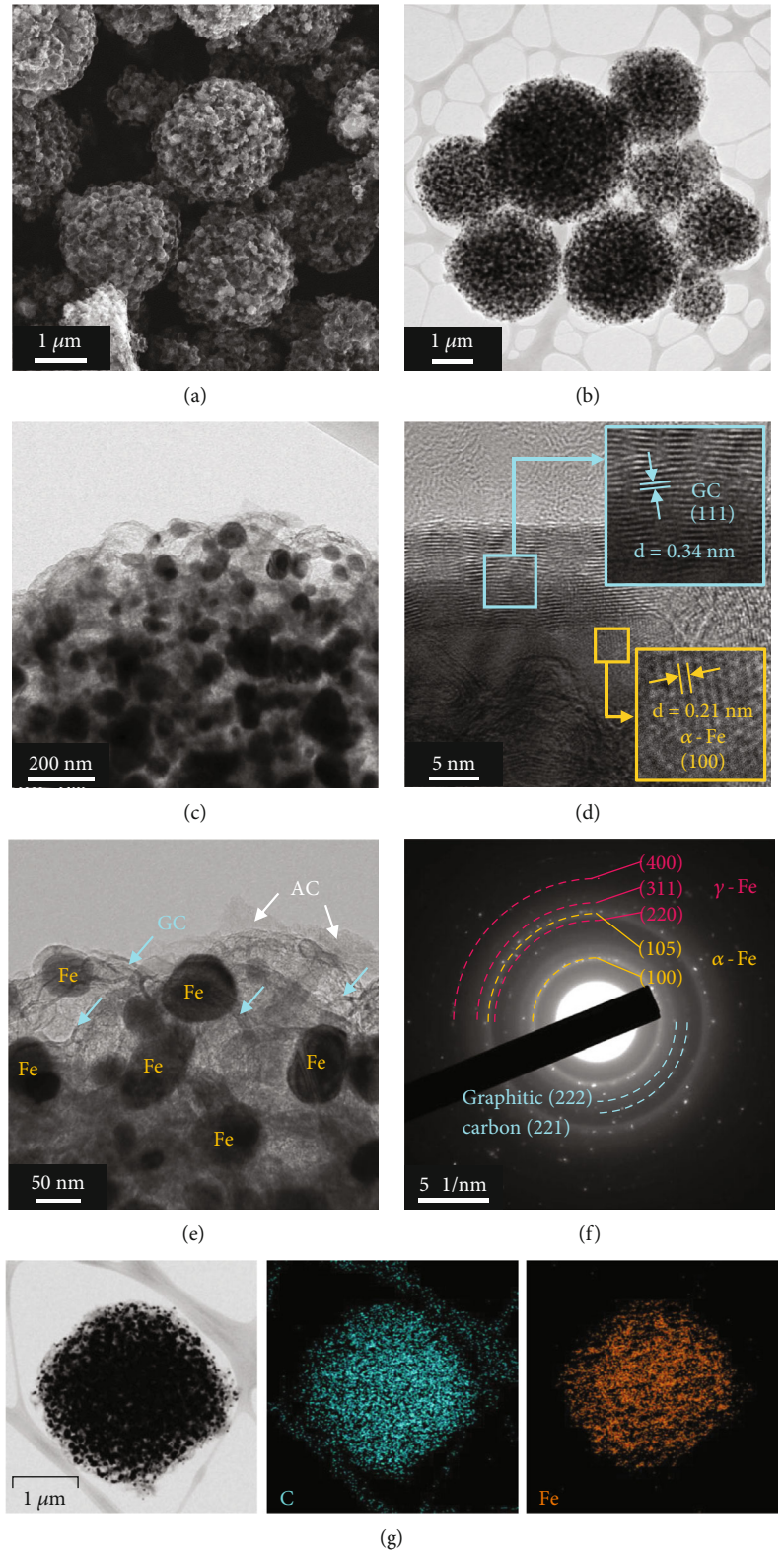

FIGURE 1: Morphological and structural characteristics of GA-HCA-Fe microspheres: (a) SEM, (b, c) TEM, (d) HR-TEM, and (e) close-up TEM images; (f) SAED pattern; and (g) elemental dot mapping images.

and the growth of Fe particles was effectively inhibited (before the outward migration). Interlayer spacing of 0.21 and 0.34 nm corresponding to the (100) plane of Fe metal and (111) plane of graphitic carbon, respectively, can be clearly discerned in the HR-TEM image (Figure 1(d)). In addition, the coexistence of amorphous carbon is observed

(top part of Figure 1(d)). The distribution of Fe particles within the microspheres can be well explained by the magnified TEM image in Figure 1(e). Notably, the shells of the hollow carbon nanospheres were composed of hollow rings; this is maybe due to the migration of Fe metal particles, which were once located inside the carbon shell, owing to the Ostwald ripening process that occurred at high temperature [49]. Therefore, the shells of each hollow carbon nanosphere are composed of onion-like graphitic carbon rings. The SAED pattern of GA-HCA-Fe microspheres shown in Figure 1(f) reveals various crystallographic rings corresponding to the (105) and (100) planes of α-Fe; the (400), (311), and (220) planes of γ-Fe; and the (222) and (221) planes of graphitic carbon, respectively. The elemental dot mapping images reveal that C and Fe are uniformly distributed in a single microsphere (Figure 1(g)).

GA-HCA-Fe microspheres were oxidized at 350°C to transform dense metallic Fe into hollow Fe_2O_3 nanospheres with high theoretical capacity and to selectively remove amorphous carbon with relatively low electrical conductivity and high initial capacity loss. To elucidate the advantages of 3D interconnected microspheres composed of highly graphitic carbon, the oxidation time was controlled (3 and 12 h) to synthesize GA-HCA-Fe_2O_3 and G-HCA-Fe_2O_3 microspheres with different amounts of amorphous carbon. The morphological traits, SAED patterns, and elemental mapping images of GA-HCA-Fe_2O_3 and G-HCA-Fe_2O_3 microspheres are shown in Figure S8 and Figure 2, respectively. The microspherical morphologies of GA-HCA-Fe_2O_3 can be ascertained from the SEM image in Figure S8a. Fe_2O_3 particles characterized by dark contrast are well distributed in the graphitic-amorphous carbon matrix, which appears to be relatively brighter (Figure S8b). Hollow Fe_2O_3 nanoparticles anchored on the carbonaceous network are observed in the close-up TEM image in Figure S8c. Nanoscale Kirkendall diffusion that results from the difference in the diffusion speed between ions occurred during oxidation process, which transformed dense metallic Fe into hollow Fe_2O_3 nanospheres [50]. It is notable that onion-like graphitic carbon rings consisting of the shell of hollow carbon nanosphere could be identified (Figure S8d), which is due to the formation of intermediate Fe metal@GC core–shell configuration during the heat treatment of iron nitrate-infiltrated HCA microspheres under Ar atmosphere. Fe metal migrated to the outside of onion-like carbon ring due to the Ostwald ripening process, leading to the formation of hollow carbon nanospheres with shells comprising onion-like graphitic carbon. Interlayer spacing of 0.27 and 0.34 nm, corresponding to (104) planes of Fe_2O_3 and (111) planes of graphitic carbon, respectively, could be ascertained in the HR-TEM image (Figure S8e). The top-right corner of the HR-TEM image also revealed the presence of amorphous carbon, which was not removed due to insufficient oxidation time. The phase analysis done by HR-TEM image was in accordance with the XRD pattern of GA-HCA-Fe_2O_3 microspheres in Figure 3(a), indicating the complete transformation of metallic Fe into Fe_2O_3 during the oxidation process. Peaks corresponding to graphitic carbon could also be observed, which corroborates that Fe_2O_3 nanoparticles are composited with graphitic carbon. The coexistence of Fe_2O_3 nanoparticles and graphitic carbon was once again substantiated with the SAED pattern (Figure S8f). As shown in the elemental mapping images (Figure S8g), Fe, O, and C elements are evenly distributed within a single microsphere.

To increase the fraction of graphitic carbon in the microspheres, GA-HCA-Fe microspheres were oxidized at 350°C for 12 h. The resultant characteristics of the prepared microspheres are presented in Figure 2. The microspherical morphology remained intact although most of the amorphous carbon was eliminated (Figures 2(a) and 2(b)). Hollow Fe_2O_3 nanospheres obtained via nanoscale Kirkendall diffusion are observed in the close-up TEM image in Figure 2(c). Hollow Fe_2O_3 nanoparticles with a void@Fe_2O_3 configuration are observed in the HR-TEM image in Figure 2(d). Furthermore, onion-like graphitic carbon, which serves as a conductive pathway for electron transport, can be observed. Thus, G-HCA-Fe_2O_3 microspheres are considered to be composed of hollow carbon nanospheres with shells consisting of onion-like graphitic carbon rings onto which hollow Fe_2O_3 nanoparticles are anchored. Notably, amorphous carbon is not observed, thereby implying that an oxidation time of 12 h removes a substantial amount of amorphous carbon. The TEM image of a fractured G-HCA-Fe_2O_3 microsphere, along with its magnified image shown in Figure S9a,b, reveals that Fe_2O_3 nanospheres are anchored to the carbon surface, as further corroborated by the elemental mapping images (Figure S9c-f). The coexistence of Fe_2O_3 phase and the graphitic carbon is observed in the XRD pattern in Figure 3(a). The SAED pattern in Figure 2(e) reveals (110), (024), (116), and (214) planes corresponding to the d-spacing of Fe_2O_3 and (101) and (111) planes relevant to graphitic carbon. The elemental dot mapping images in Figure 2(f) reveal that iron oxide nanoparticles are well distributed within the 3D graphitic carbon matrix. The overlapped elemental mapping image of G-HCA-Fe_2O_3 microspheres is provided in Figure S10, which clearly revealed the distribution of each element. To investigate the universality of this synthetic strategy, GA-HCA-Ni microspheres were prepared by infiltration of nickel nitrate into HCA microspheres and subsequent heat treatment under Ar atmosphere (900°C). The SEM images of GA-HCA-Ni (Figure S11a) microspheres bore resemblance to its GA-HCA-Fe counterpart. The XRD pattern of the prepared powder in Figure S11b exhibited a peak at 26.6°, revealing the successful formation of graphitic carbon.

To elucidate the role of the 3D conductive G-HCA matrix in the electrochemical properties, carbon-free 3D porous Fe_2O_3 microspheres were also prepared by oxidizing iron nitrate-infiltrated HCA microspheres at 350°C for 12 h. The morphologies, SAED pattern, and the elemental mapping images are provided in Figure S12; the prepared microspheres exhibited spherical morphologies, which can be confirmed from the SEM image in Figure S12a. The TEM image in Figure S12b well elucidates the 3D porous morphology of the prepared powder. The XRD pattern of the carbon-free microspheres (Figure 3(a)) reveals broad

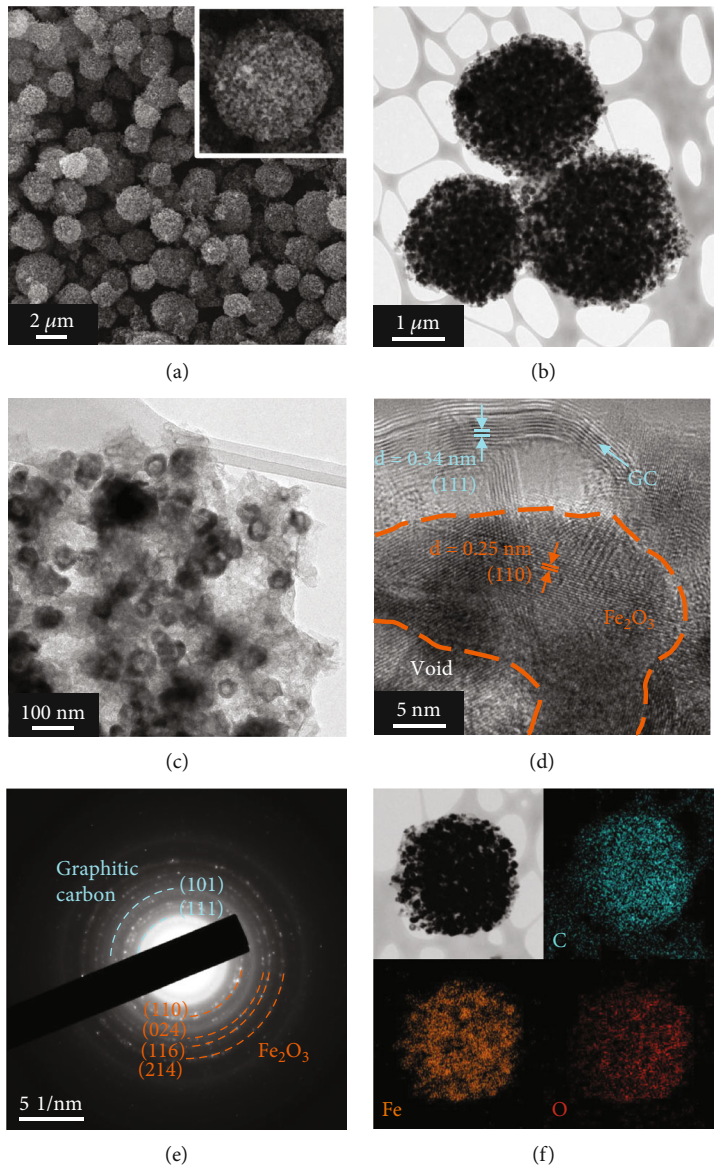

FIGURE 2: Morphological and structural characteristics of G-HCA-Fe_2O_3 microspheres: (a) SEM, (b, c) TEM, and (d) HR-TEM images; (e) SAED pattern; and (f) elemental dot mapping images.

peaks corresponding to the Fe_2O_3 phase, implying that the crystallite size is considerably small. This is in line with the close-up TEM image shown in Figure S12c where the small Fe_2O_3 nanocrystals comprising the porous microsphere could be well discerned. Interlayer spacing of 0.22 and 0.25 nm and various crystallographic rings with d-spacing in the HR-TEM image and SAED pattern in Figure S12d,e ascertains the formation of Fe_2O_3 phase. The elemental mapping images reveal the existence of Fe and O elements; C element was eliminated due to the combustion of amorphous carbon (Figure S12f). Digital photographs of powder corresponding to carbon-free Fe_2O_3 and G-HCA-Fe_2O_3 microspheres are shown in Figure S13. The carbon-free Fe_2O_3 microspheres present a reddish color, which is a typical indication for Fe_2O_3-based materials (Figure S13a). The oxidation of iron nitrate-infiltrated HCA microspheres comprised of amorphous carbon at 350°C for 12 h resulted in the complete elimination of carbon. In contrast, heat treatment of iron nitrate-infiltrated HCA microspheres under Ar atmosphere during the preparation of G-HCA-Fe_2O_3 microspheres successfully transformed some amorphous carbon into graphitic carbon with higher thermal stability. Therefore, G-HCA-Fe_2O_3 microspheres that are comprised mainly of graphitic carbon exhibited black color originating from graphitic carbon material (Figure S13b).

The X-ray photoelectron spectroscopy (XPS), thermogravimetric analysis (TGA), Raman analysis, and electrochemical impedance spectroscopy (EIS) were used to track the changes in the material characteristics of GA-HCA-Fe, GA-HCA-Fe_2O_3, G-HCA-Fe_2O_3, and carbon-free Fe_2O_3 microspheres, and their results are presented in Figure 3. The core-level XPS spectra of the samples are provided in Figures 3(b)–3(d) and S14. The C 1 s XPS spectra shown in

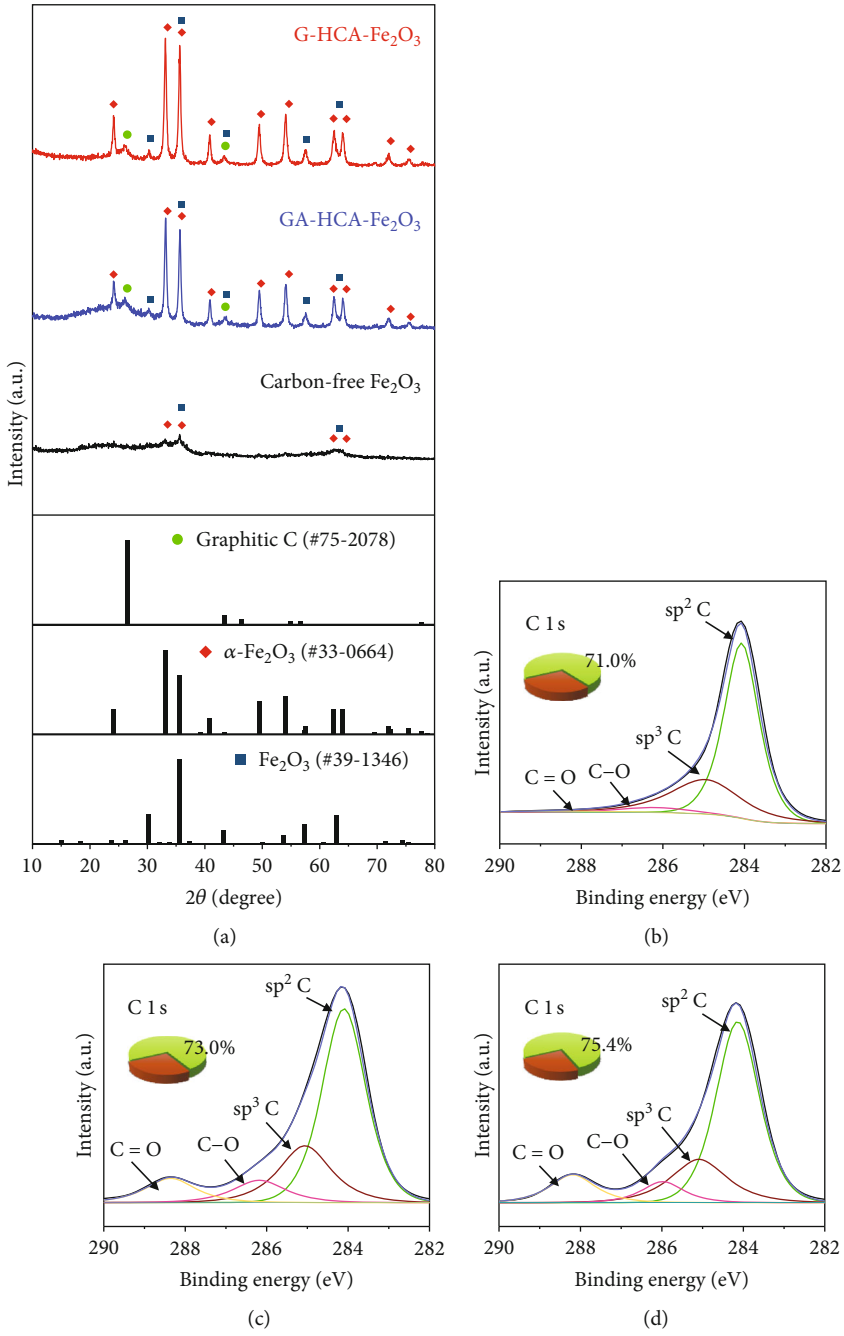

Figure 3: Continued.

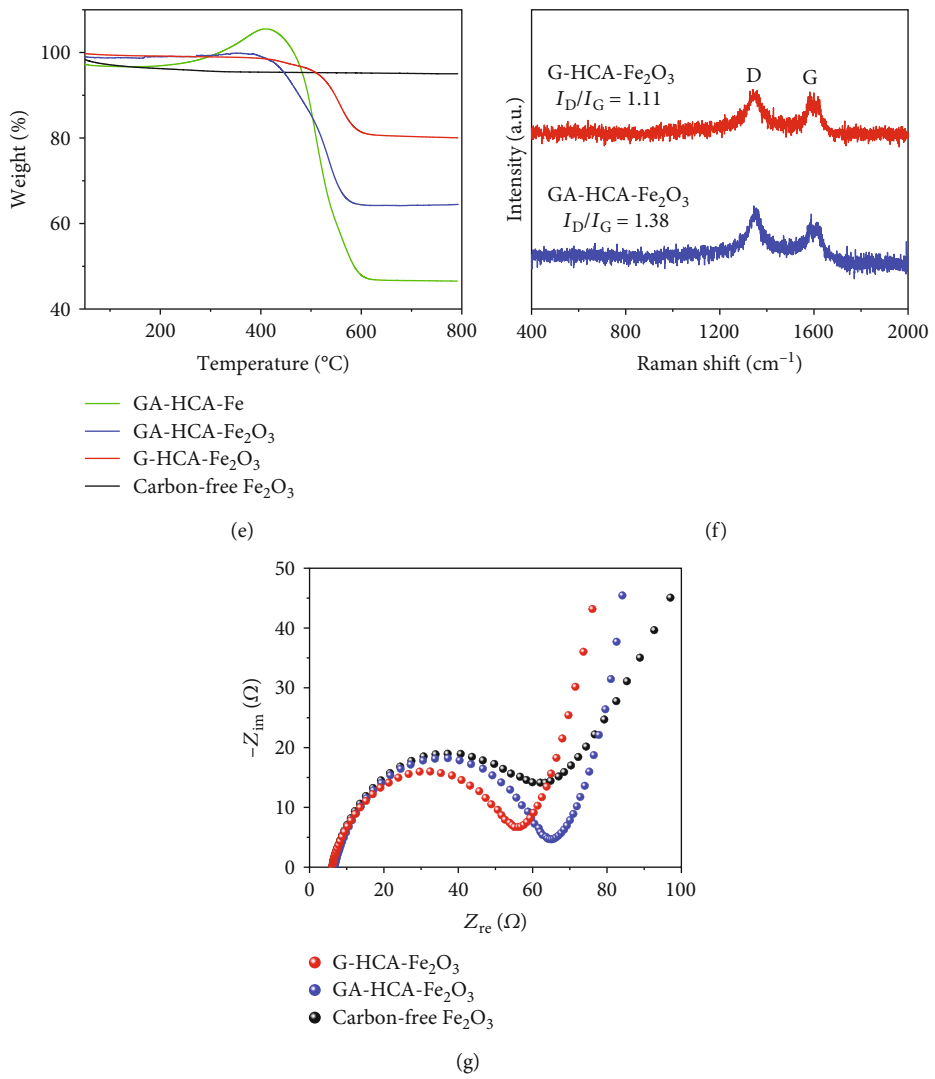

Figure 3: Material characterization of GA-HCA-Fe, GA-HCA-Fe_2O_3, G-HCA-Fe_2O_3, and carbon-free Fe_2O_3 microspheres: (a) XRD patterns; (b–d) C 1 s XPS spectra of GA-HCA-Fe, GA-HCA-Fe_2O_3, and G-HCA-Fe_2O_3 microspheres; (e) TGA curves; (f) Raman spectra; and (g) EIS Nyquist plot for the freshly assembled cells.

Figures 3(b)–3(d) reveal four peaks at 284.1, 285.1, 286.2, and 288.4 eV, corresponding to sp^2 carbon, sp^3 carbon, and C–O and C=O bonds, respectively [51, 52]; sp^2 carbon and sp^3 carbon correspond to graphitized and amorphous carbon, respectively, and the area under the peaks can be used to determine their percentages [52]. The percentages of sp^2 carbon in GA-HCA-Fe, GA-HCA-Fe_2O_3, and G-HCA-Fe_2O_3 microspheres are 71.0, 73.0, and 75.4%, respectively, with increasing oxidation time. The percentage of sp^3 carbon appears to be high even after oxidation since carbon tape was used for the XPS analysis, but the increasing trend of the percentage of sp^2 carbon was conspicuous. This result demonstrates that the amorphous carbon could be removed during the oxidation in a time-wise manner. In the TGA analysis shown in Figure 3(e), the weight of GA-HCA-Fe microspheres increases starting from 300°C, and this is attributed to the transformation of metallic Fe into Fe_2O_3. The theoretical weight increase during the phase change is approximately 43 wt%, but the y value does not reach 143 wt% due to the weight loss corresponding to the combustion of the carbonaceous material near the similar temperature. The total amorphous and graphitic carbon content in GA-HCA-Fe microspheres calculated from the TGA curves is 67.4 wt%. For GA-HCA-Fe_2O_3 and G-HCA-Fe_2O_3 microspheres, the carbon material contents calculated from TGA curves are 35.5 and 19.7 wt%, respectively. The result shows that more amorphous carbon is included in GA-HCA-Fe_2O_3 microspheres, indicating that oxidation time (3 h) was insufficient to remove all amorphous carbon. The TGA curve of carbon-free Fe_2O_3 microspheres was also obtained, where no weight fluctuation above 250°C was observed; the weight loss below the specific temperature may be due to the water species adsorbed on the surface of the sample. The Fe 2p and O 1 s XPS spectra of GA-HCA-Fe, GA-HCA-Fe_2O_3, G-HCA-Fe_2O_3, and carbon-free Fe_2O_3 microspheres are shown in Figure S14. Fe $2p_{3/2}$ and Fe $2p_{1/2}$ regions in the Fe 2p spectrum of GA-HCA-Fe microspheres (Figure S14a) can be deconvoluted into four

peaks at 706.6/719.5, 709.8/722.9, 712.1/724.5, and 716.1/726.7 eV corresponding to metallic Fe, Fe^{2+}, Fe^{3+}, and satellites, respectively [53, 54]. Owing to the heat treatment of iron-salt-impregnated HCA microspheres under an Ar atmosphere, metallic Fe particles were formed, as determined using the XRD pattern shown in Figure S6. Fe^{2+} and Fe^{3+} oxidation states can be observed because of surface oxidation due to exposure to air. GA-HCA-Fe_2O_3, G-HCA-Fe_2O_3, and carbon-free Fe_2O_3 microspheres exhibited peaks corresponding to Fe^{2+} and Fe^{3+} oxidation states and their satellites (Figure S14c,e,g). In the O 1 s spectra of all samples (Figure S14b,d,f,h), three peaks centered at 529.5, 531.4, and 532.7 eV can be assigned to the lattice oxygen (Fe–O), surface hydroxyl group (–OH), and adsorbed water (H_2O), respectively [55]. Raman spectroscopy was performed to compare the degree of graphitization of carbon in G-HCA-Fe_2O_3 and GA-HCA-Fe_2O_3 microspheres (Figure 3(f)). The peaks at 1350 and 1590 cm^{-1} are related to the D-band (amorphous carbon) and G-band (graphitic carbon) of carbon materials, respectively [56–59]. The I_D/I_G values can be used to understand the degree of graphitization, which were calculated as 1.11 and 1.38 for G-HCA-Fe_2O_3 and GA-HCA-Fe_2O_3 microspheres, respectively, indicating that the carbon in G-HCA-Fe_2O_3 microspheres exhibits a higher degree of graphitization [60]. This suggests that amorphous carbon can be selectively removed during oxidation at 350°C. Furthermore, EIS was used to evaluate the charge-transfer resistance of GA-HCA-Fe_2O_3, G-HCA-Fe_2O_3, and carbon-free Fe_2O_3 microspheres. The Nyquist plots obtained after cell assembly were deconvoluted using the Randles-type equivalent circuit model in Figure S15; the depressed semicircle at relatively high frequencies can be used to calculate the charge-transfer resistance (R_{ct}) [61–64]. The R_{ct} values for G-HCA-Fe_2O_3, GA-HCA-Fe_2O_3, and carbon-free Fe_2O_3 microspheres are 49, 58, and 62 Ω, respectively. G-HCA-Fe_2O_3 and GA-HCA-Fe_2O_3 microspheres exhibited lower resistance in comparison to carbon-free Fe_2O_3 microspheres since they are composited with 3D porous carbon matrix which acts as a conductive pathway for electrons. The lower R_{ct} value of G-HCA-Fe_2O_3 microspheres in comparison to GA-HCA-Fe_2O_3 microspheres is probably due to the higher degree of graphitic carbon with high electrical conductivity in G-HCA-Fe_2O_3 microspheres. The electrical conductivity of G-HCA-Fe_2O_3 microspheres measured from four-point probe method was 6.1×10^{-2} S m^{-1}. The surface areas and porosity profiles of the samples were analyzed using the Brunauer–Emmett–Teller method (Figure S16). From the N_2 adsorption/desorption isotherms, the specific surface areas of G-HCA-Fe_2O_3, GA-HCA-Fe_2O_3, and carbon-free Fe_2O_3 microspheres are determined as 81, 119, and 61 $m^2 g^{-1}$, respectively. G-HCA-Fe_2O_3 microspheres exhibited smaller specific surface area in comparison to GA-HCA-Fe_2O_3 microspheres, which can be attributed to the lower content of carbon with higher specific surface area in comparison to Fe_2O_3 material. In addition, graphitization of carbon is known to result in the coalescence of pores in amorphous carbon [65]. Therefore, G-HCA-Fe_2O_3 microspheres with smaller amount of carbon with highly graphitic nature probably exhibited a smaller specific surface area. Both G-HCA-Fe_2O_3 and GA-HCA-Fe_2O_3 microspheres exhibited a type IV isotherm, indicating the presence of mesopores in carbon materials. Carbon-free Fe_2O_3 microspheres also exhibit a high specific surface area owing to the porous internal nanostructure. The BJH pore size distribution revealed the presence of pores ~3 nm, which is in line with the TEM image in Figure S12c revealing the presence of pores between the Fe_2O_3 particles.

The electrochemical properties of G-HCA-Fe_2O_3, GA-HCA-Fe_2O_3, and carbon-free Fe_2O_3 microspheres were analyzed (Figure 4). Cyclic voltammograms (CVs) of G-HCA-Fe_2O_3, GA-HCA-Fe_2O_3, and carbon-free Fe_2O_3 microspheres obtained for the first 5 cycles at a sweep rate of 0.1 mV s^{-1} in the voltage window of 0.001-3.0 V are shown in Figure 4(a) and S17. Considerable differences in the first and subsequent cycles could be observed, which indicates an irreversible phase transformation during the insertion/extraction process in the first cycle. In the case of G-HCA-Fe_2O_3 microspheres, during the initial cathodic scan, the main reduction peaks were observed at 1.6 V and 0.7 V (Figure 4(a)). The peaks at 1.6 V and 0.7 V are associated with the insertion of Li^+ into Fe_2O_3 ($Fe_2O_3 + xLi^+ + xe^- \rightarrow Li_xFe_2O_3$) and the conversion reaction of $Li_xFe_2O_3$ to metallic Fe along with the formation of solid electrolyte interphase (SEI) layer on the electrode surface, respectively [66, 67]. According to the literature, the minor peak at approximately 1.0 V may be ascribed to the partial phase transition from hexagonal $Li_xFe_2O_3$ to cubic $Li_2Fe_2O_3$ upon additional Li uptake [67, 68]. A sharp cathodic peak is observed near 0 V, which is attributed to the intercalation of Li^+ in the graphitic carbon layer [69]. In the first anodic scan, a peak at 0.1 V is associated with the deintercalation of Li^+ from the carbon layer [69]. In addition, two peaks at 1.6 V and 1.85 V could be observed, which are attributed to the oxidation reactions corresponding to the transformation from metallic Fe to Fe^{2+} and Fe^{2+} to Fe^{3+}, respectively [70]. In the subsequent cycles, some cathodic peaks disappear and develop into a peak at approximately 0.8 V, which corresponds to the reversible conversion reaction that leads to the complete transition to metallic Fe [67]. The CV profiles are considerably overlapped, implying that highly reversible electrochemical reactions occur during the charge–discharge processes. The CV curves of GA-HCA-Fe_2O_3 microspheres in Figure S17a are analogous to those of G-HCA-Fe_2O_3 microspheres, demonstrating a similar electrochemical reaction mechanism. However, slight differences are observed; for instance, the peak intensity of the conversion reaction at around 0.7 V was decreased due to the presence of amorphous carbon and the relatively lower amount of Fe_2O_3 than G-HCA-Fe_2O_3 microspheres as proven by the TGA results (Figure 3(e)). For the CV curves of carbon-free Fe_2O_3 microspheres in Figure S17b, the peak at approximately 0 V, which is attributed to graphitic carbon materials, is not observable. Galvanostatic charge–discharge curves of G-HCA-Fe_2O_3, GA-HCA-Fe_2O_3, and carbon-free Fe_2O_3 microspheres obtained at 1.0 A g^{-1} are shown in Figure 4(b). During the first discharge, a distinct plateau is

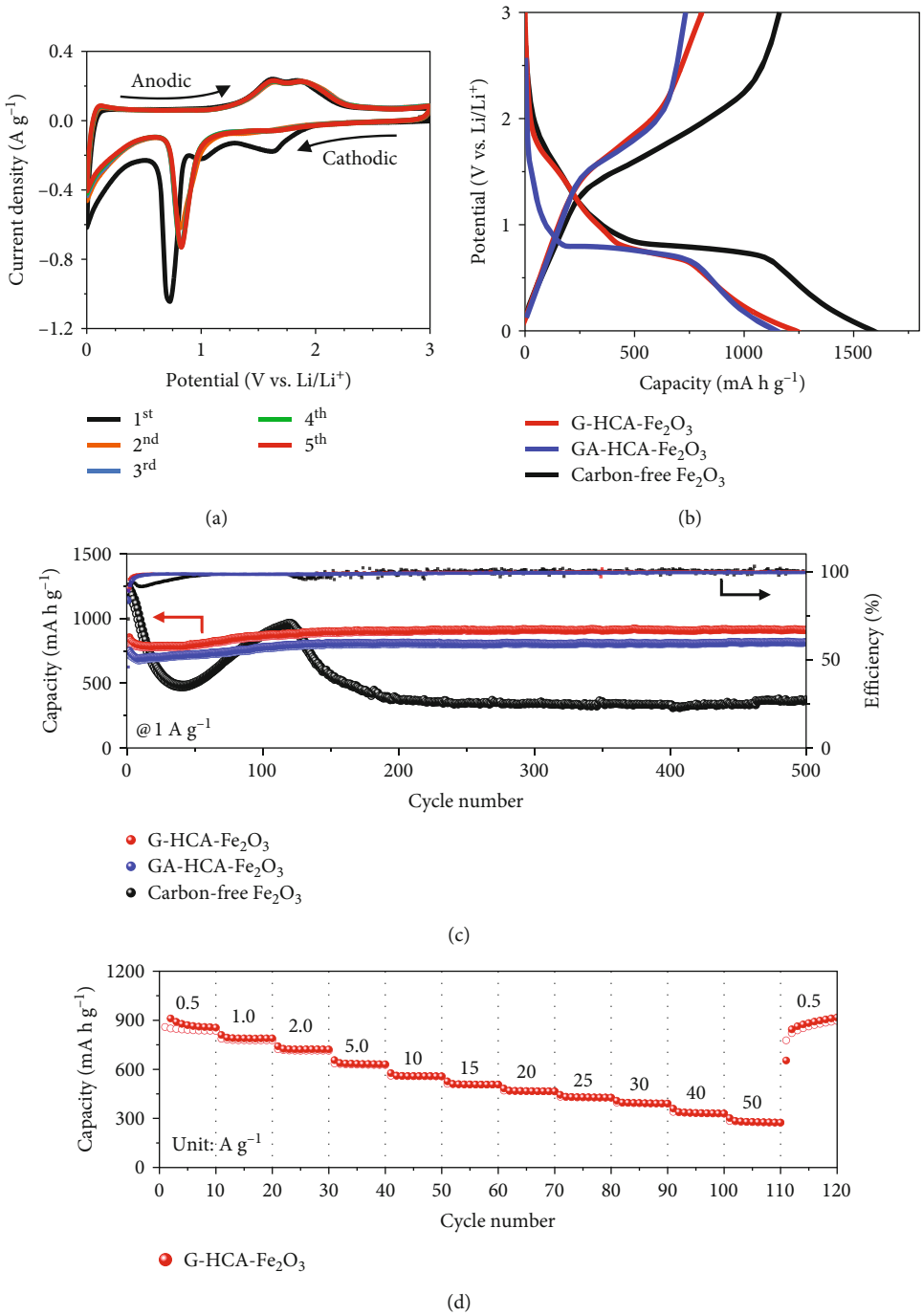

Figure 4: Continued.

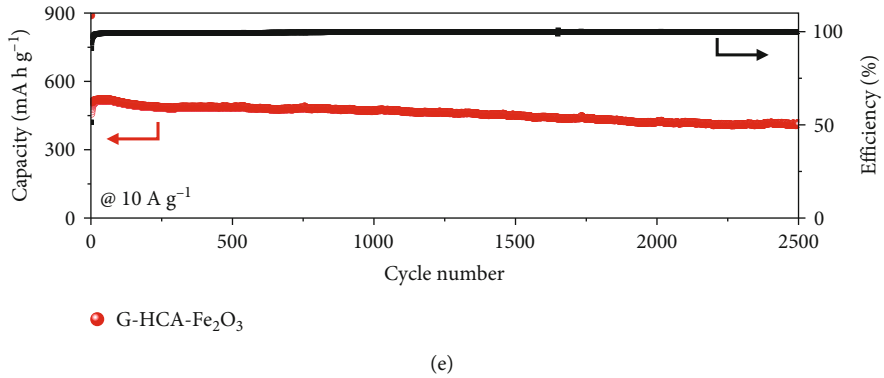

(e)

Figure 4: Electrochemical properties of G-HCA-Fe_2O_3, GA-HCA-Fe_2O_3, and carbon-free Fe_2O_3 microspheres: (a) CV curves of G-HCA-Fe_2O_3 microspheres, (b) charge-discharge profiles at 1.0 A g^{-1} for the initial cycle, (c) cycle performance at 1.0 A g^{-1}, (d) rate performance, and (e) long-term cycle performance at 10.0 A g^{-1}.

observed at around 0.72 V, which agrees with the potential at which the main conversion reaction occurs in CV curves [67]. The slopy plateau of G-HCA-Fe_2O_3 and GA-HCA-Fe_2O_3 microspheres at around 0 V is attributed to the intercalation of Li^+ into the graphitic carbon layer [69]. The initial discharge capacities of G-HCA-Fe_2O_3, GA-HCA-Fe_2O_3, and carbon-free Fe_2O_3 microspheres are 1236, 1142, and 1589 mA h g^{-1}, respectively, and their initial Coulombic efficiencies (ICE) are 65.3, 63.8, and 73.0%. G-HCA-Fe_2O_3 and GA-HCA-Fe_2O_3 microspheres exhibit lower ICE values in comparison to carbon-free Fe_2O_3 microspheres owing to the presence of carbon, which are characterized by low ICE. The slightly higher ICE for G-HCA-Fe_2O_3 microspheres than GA-HCA-Fe_2O_3 microspheres is attributed to the lower carbon content. It can be also explained by the fact that amorphous carbon generally exhibits lower ICE in comparison to graphitic carbon [71]. The cycling performances of the three electrodes at a current density of 1.0 A g^{-1} are shown in Figure 4(c); G-HCA-Fe_2O_3 microspheres exhibited stable cycle performance, where a reversible capacity of 914 mA h g^{-1} was delivered for the 500th cycle. GA-HCA-Fe_2O_3 microspheres also exhibited high structural robustness and showed capacity of 818 mA h g^{-1} after 500 cycles. From such cycling performances, it can be deduced that the design of such carbon-composited 3D porous structure efficiently reinforced the overall structural stability, leading to excellent electrochemical performances. The reason for the stable cycle performance of both G-HCA-Fe_2O_3 and GA-HCA-Fe_2O_3 microspheres can be attributed to the unique structure of the 3D porous carbonaceous matrix, where hollow Fe_2O_3 nanoparticles are anchored on the surface of the inner shell of each hollow nanosphere subunit. The matrix could not only enhance the electrical conductivity but also buffer the volumetric variation of numerous hollow Fe_2O_3 nanospheres during charge–discharge process. The hollow interior of Fe_2O_3 nanospheres itself could also effectively accommodate the stress received during repetitive cycles. In addition, G-HCA-Fe_2O_3 microspheres delivered higher capacities than GA-HCA-Fe_2O_3 microspheres due to the lower amount of amorphous carbon present in the composite electrode as well as higher portion of onion-like graphitic carbon rings that provided electron transportation channel. In the case of carbon-free Fe_2O_3 microspheres comprised of porous Fe_2O_3 nanoparticles, the anode exhibits a higher capacity in comparison to G-HCA-Fe_2O_3 and GA-HCA-Fe_2O_3 microspheres because it is not composited with carbon species. However, the anode undergoes severe capacity fading during the initial 40 cycles, since it could not endure the huge volume changes due to the absence of the 3D porous carbon shielding that can effectively prevent the pulverization of electrode. The rate performances of G-HCA-Fe_2O_3, GA-HCA-Fe_2O_3, and carbon-free Fe_2O_3 microspheres tested at various current densities are presented in Figure 4(d) and Figure S18. G-HCA-Fe_2O_3 microspheres exhibit reversible capacities of 855, 789, 722, 631, 557, 506, 465, 426, 390, 329, and 274 mA h g^{-1} at current densities of 0.5, 1.0, 2.0, 5.0, 10, 15, 20, 25, 30, 40, and 50 A g^{-1}, respectively (Figure 4(d)). In the case of rate performance of GA-HCA-Fe_2O_3 microspheres shown in Figure S18, reversible capacities of 811, 735, 657, 557, 484, 434, 390, 351, 316, 258, and 209 mA h g^{-1} were delivered at the same current densities. The capacity gaps between G-HCA-Fe_2O_3 and GA-HCA-Fe_2O_3 clearly demonstrate that the difference in the degree of graphitization in the composite anode causes difference in electrical conductivity, which affected the rate capability of the electrode materials. When the current density is restored to 0.5 A g^{-1}, G-HCA-Fe_2O_3 displays a discharge capacity of 916 mA h g^{-1}, which is comparable to the initial reversible capacity at the same rate. For carbon-free Fe_2O_3 microspheres, the capacity decreases from 1165 to 26 mA h g^{-1} when the current density is changed from 0.5 to 50.0 A g^{-1}. Although the anode is characterized by small Fe_2O_3 nanoparticles interspersed with small pores, which generally results in a good rate capability, high capacities could not be retained at an ultrahigh current density of 50.0 A g^{-1}. The degree of voltage gap widening in G-HCA-Fe_2O_3 microspheres with changes in current density was lower than that of GA-HCA-Fe_2O_3 and carbon-free Fe_2O_3 microspheres, indicating the lower degree of polarization changes (Figure S19). The remarkable rate performance of G-HCA-Fe_2O_3 microspheres can be attributed to the highly conductive 3D porous graphitic carbon microspheres, which allow higher electrical

conductivity and facile electrolyte penetration into the electrode. Furthermore, hollow Fe_2O_3 nanoparticles anchored on the conductive carbon matrix, which are formed by nanoscale Kirkendall diffusion, effectively reduced the lithium-ion diffusion path and accelerated the electrochemical kinetics. To clearly demonstrate the roles of compositing graphitic carbon matrix and the degree of graphitization in the carbon materials, the rate capability of the three samples was also compared using retained capacity (%) vs. current density (Figure S20) since their absolute capacities are different. The long-term cycle stability tests of G-HCA-Fe_2O_3, GA-HCA-Fe_2O_3, and carbon-free Fe_2O_3 microspheres were carried out at a high current density of 10.0 A g^{-1}, and the results are shown in Figure 4(e) and Figure S21. For G-HCA-Fe_2O_3 microspheres, the capacity increases during the first 50 cycles owing to the progressive activation of the porous electrode materials at high current densities. The electrode exhibits superior long-term cycle stability, where a reversible capacity of 410 mA h g^{-1} for the 2500th cycle was obtained and the capacity retention measured from the 50th cycle was 78.6%. The long-term cycle performances of GA-HCA-Fe_2O_3 and carbon-free Fe_2O_3 at 10 A g^{-1} are shown in Figure S21; reversible capacity of 261 mA h g^{-1} was delivered after the 1500th cycle in the case of GA-HCA-Fe_2O_3 microspheres. The capacities of carbon-free Fe_2O_3 microspheres dropped dramatically, which ascertains that HCA microspheres play a critical role in terms of cycle stability. The results demonstrate that the unique nanostructure of the anode composited with a highly conductive graphitic carbon matrix endows long-term cycle stability even at a high current density of 10 A g^{-1}. To confirm the structural advantages of G-HCA-Fe_2O_3 microspheres, the thickness of the prepared electrodes before and after the cycling test (100 cycles at 10 A g^{-1}) was measured. The thickness of electrodes comprising G-HCA-Fe_2O_3 microspheres increased from 17.2 to 17.5 μm, whereas that comprising carbon-free Fe_2O_3 microspheres increased from 16.1 to 41.3 μm (Figure S22). The electrochemical performance of G-HCA-Fe_2O_3 microspheres was compared with Fe_2O_3 material-based materials as well as hollow metal oxide nanospheres with similar morphology applied as anodes for LIBs (Table S1,2). Carefully designed G-HCA-Fe_2O_3 microspheres with well-defined nanostructure, aimed at achieving high electrochemical performance at high charge rate, showed superior lithium-ion storage characteristics among the various anode materials. To confirm the role of G-HCA in G-HCA-Fe_2O_3 microspheres, G-HCA was prepared from etching out Fe_2O_3 in G-HCA-Fe_2O_3 microspheres with hydrochloric acid. G-HCA powder exhibited lower capacities in comparison to G-HCA-Fe_2O_3 microspheres, but the cycle performance was highly stable (Figure S23). Therefore, it can be assumed that the high capacity is derived from Fe_2O_3 material with high theoretical capacity and the structural robustness is provided by G-HCA matrix. The reversible capacities of G-HCA decreased from 434.8 to 40.6 mA h g^{-1} when the current density is increased from 0.5 to 50.0 A g^{-1}. The capacity is rather low, but as will be demonstrated by the surface kinetics analysis in Figure 5, it allows highly surface-capacitive reaction, resulting in high rate performance of G-HCA-Fe_2O_3 microspheres.

To understand the origin of the high rate capability of G-HCA-Fe_2O_3 microspheres, CV curves at various sweep rates from 0.1 to 2.0 mV s^{-1} were obtained to understand the electrochemical kinetics, as shown in Figures 5(a)–5(c). The relationship between the obtained peak current (i) and sweep rate (v) can be described by the power law, as follows [72, 73]:

$$i = av^b, \tag{1}$$

$$\log i = \log a + b \log v. \tag{2}$$

After applying logarithms to both sides of Equation (1), the b value can be obtained by linearly fitting log a versus log v (Equation (2)). The b value indicates whether the diffusion-limited element or the surface-capacitive element is dominant in electrochemical reactions [72, 73]. Specifically, a b value approaching 0.5 indicates that the diffusion-limited reaction is dominant, whereas a value approaching 1 implies that the surface-capacitive reaction predominantly occurs. The b values for peaks 1 (anodic) and 2 (cathodic) of each sample, where the main electrochemical reactions occur, are calculated as shown in Figures 5(d)–5(f). The b value significantly differs depending on the existence of the 3D porous carbon matrix. G-HCA-Fe_2O_3 and GA-HCA-Fe_2O_3 microspheres composited with carbon exhibit considerably higher b values than that of carbon-free Fe_2O_3 microspheres, which exhibit relatively low b values of 0.678 and 0.462. G-HCA-Fe_2O_3 microspheres exhibited higher b value in comparison to GA-HCA-Fe_2O_3 microspheres, which can be attributed to the higher degree of graphitic carbon with high electrical conductivity. Furthermore, the degree of surface-capacitive and diffusion-limited elements can be quantitatively distinguished using the following equation [74, 75]:

$$i = k_1 v + k_2 v^{1/2}. \tag{3}$$

In Equation (3), the first ($k_1 v$) and second ($k_2 v^{1/2}$) terms imply surface-capacitive and diffusion-limited contributions, respectively. The capacitive contribution analyzed at various sweep rates is shown in Figures 5(g)–5(i). Carbon-free Fe_2O_3 microspheres exhibit much lower surface-capacitive contribution than those of G-HCA-Fe_2O_3 and GA-HCA-Fe_2O_3 microspheres with graphitic carbon, indicating that the existence of a conductive carbon matrix considerably influences the surface-capacitive reaction kinetics during the charge–discharge process. For example, at a sweep rate of 2.0 mV s^{-1}, G-HCA-Fe_2O_3, GA-HCA-Fe_2O_3, and carbon-free Fe_2O_3 microspheres exhibit surface-capacitive contributions of 96, 91, and 62%, respectively, with reference to the empirically obtained current (Figure S24). G-HCA-Fe_2O_3 microspheres exhibit a higher percentage of capacitive elements than GA-HCA-Fe_2O_3 microspheres, demonstrating that the degree of graphitization of the carbon material significantly affects the acceleration of the

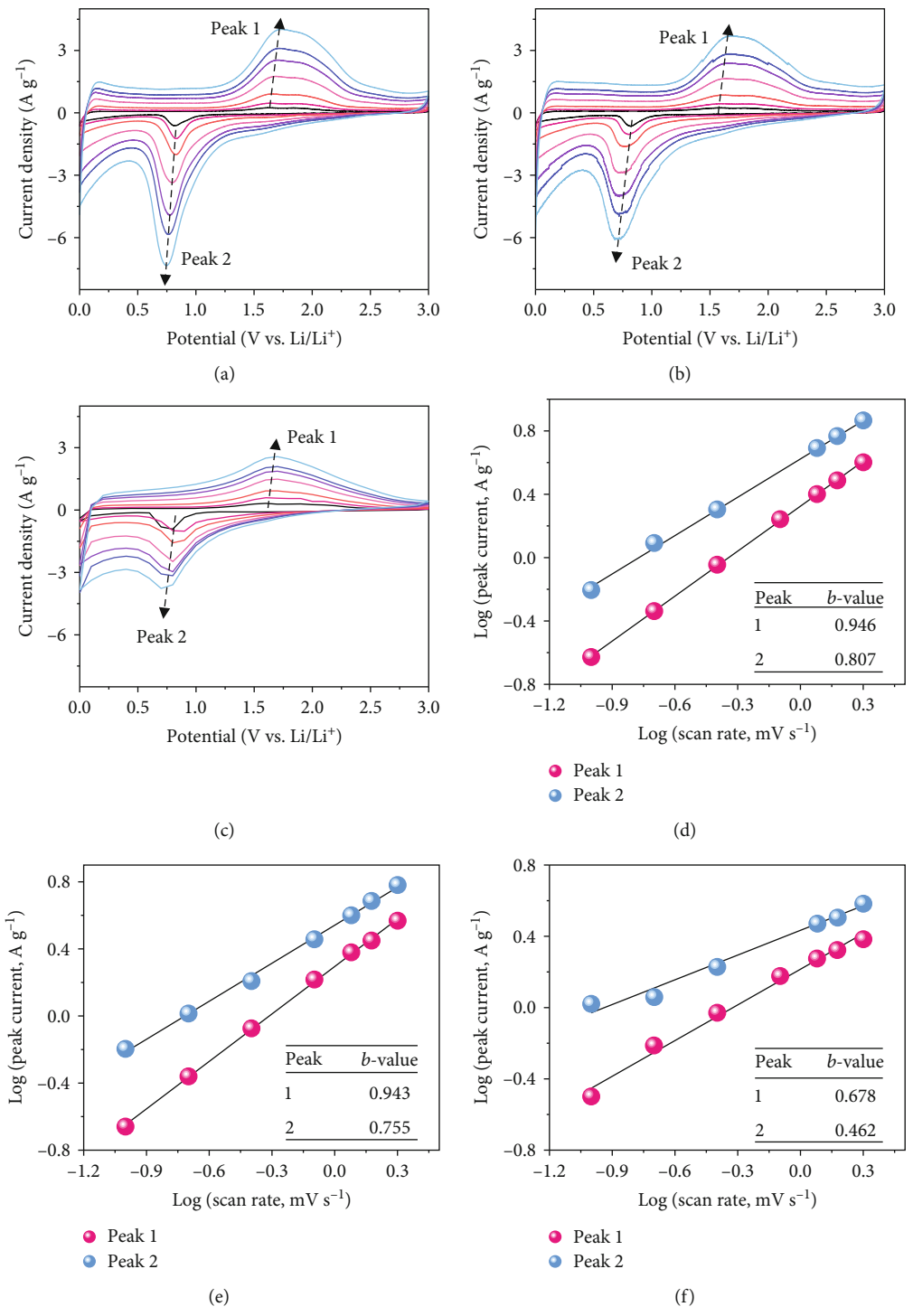

Figure 5: Continued.

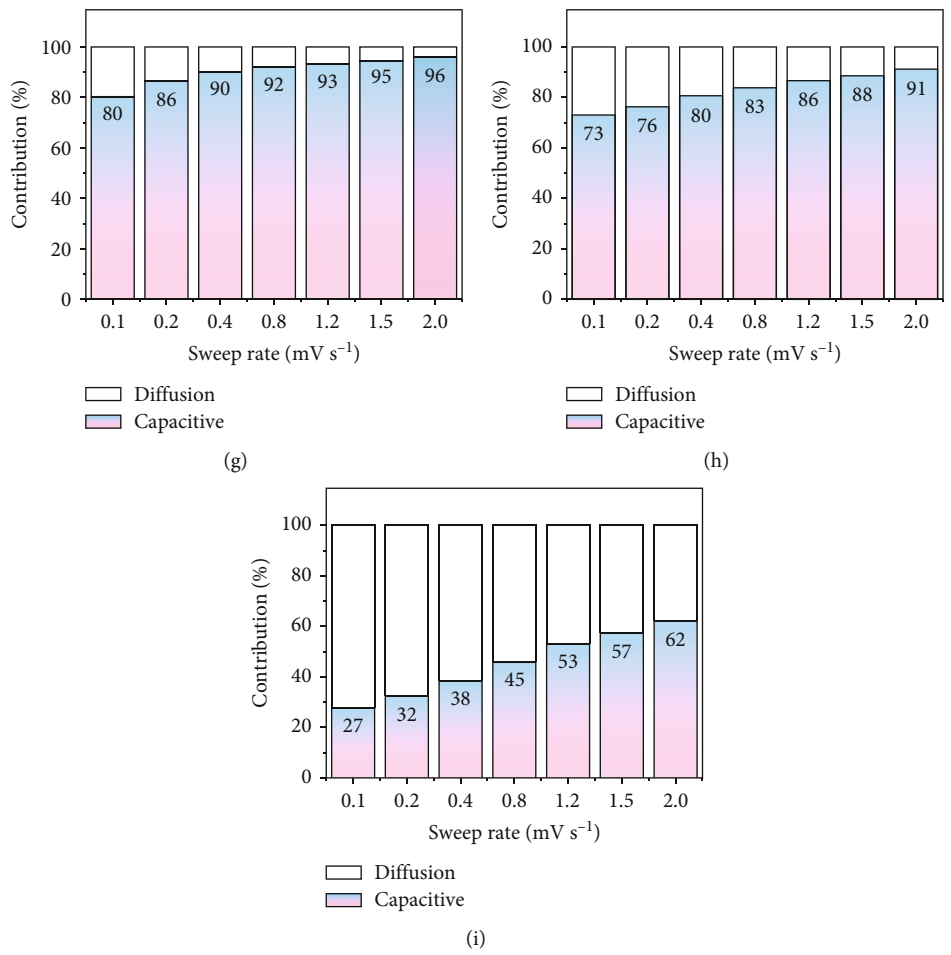

Figure 5: Electrochemical reaction kinetics analysis: (a–c) CV curves obtained at various sweep rates, (d–f) fitted log (peak current) vs. log (scan rate), and (g–i) capacitive contribution at various sweep rates for (a, d, and g) G-HCA-Fe_2O_3, (d–f) GA-HCA-Fe_2O_3, and (g–i) carbon-free Fe_2O_3 microspheres.

electrochemical kinetics, which is consistent with the results of the rate capability test results.

To identify the cause of the stable cycle performance and the high electrochemical kinetics of G-HCA-Fe_2O_3 microspheres in comparison to GA-HCA-Fe_2O_3 and carbon-free Fe_2O_3 microspheres, ex situ EIS Nyquist plots for the 1st, 100th, and 400th cycles (Figures 6(a)–6(c)) and ex situ SEM images after 400 cycles at 1.0 A g^{-1} (Figures 6(d)–6(f)) were obtained. As mentioned previously (Figure 3(g)), considering the newly assembled cell, the R_{ct} values for G-HCA-Fe_2O_3 microspheres are lower than those for GA-HCA-Fe_2O_3 and carbon-free Fe_2O_3 microspheres. The Nyquist plots of the samples after the initial cycle shown in Figure 6(a) reveal that R_{ct} values decreased to a large extent due to the formation of ultrafine nanocrystals. From the 1st cycle and onward, another semicircle at higher frequency could be observed, which corresponds to the resistance arising from SEI film formed at the surface (R_f). After 100 cycles, G-HCA-Fe_2O_3 and GA-HCA-Fe_2O_3 microspheres exhibited much lower resistance in comparison to carbon-free Fe_2O_3, indicating the structural destruction of carbon-free Fe_2O_3 during repetitive cycling. The R_f/R_{ct} values of G-HCA-Fe_2O_3, GA-HCA-Fe_2O_3, and carbon-free Fe_2O_3 microspheres after 400 cycles at 1.0 A g^{-1} were 4/18, 18/38, and 44/76 Ω, respectively. R_f/R_{ct} values were especially small in the case of G-HCA-Fe_2O_3 microspheres which implies the structural robustness of the electrode as well as stable SEI layer formation on the surface. For better understanding, various battery parameters obtained from the Nyquist plots using Zview software are summarized in Table S3 [76–81]. The after-cycle SEM image of G-HCA-Fe_2O_3 microspheres in Figure 6(d) reveals that spherical morphology was well maintained, and the small individual primary hollow carbon nanospheres constituting the microspheres were well discerned. This indicates that the 3D porous conductive highly graphitic carbon matrix and hollow Fe_2O_3 nanospheres anchored on the surface played an effective role in alleviating the volume changes during cycling and preventing the pulverization of the electrode material. GA-HCA-Fe_2O_3 microspheres also retained their microspherical morphologies well even after 400 cycles, but some type of coating layer relevant to the SEI materials could be observed at the surface (Figure 6(e)). In the case of carbon-free Fe_2O_3 microspheres, structural deformation

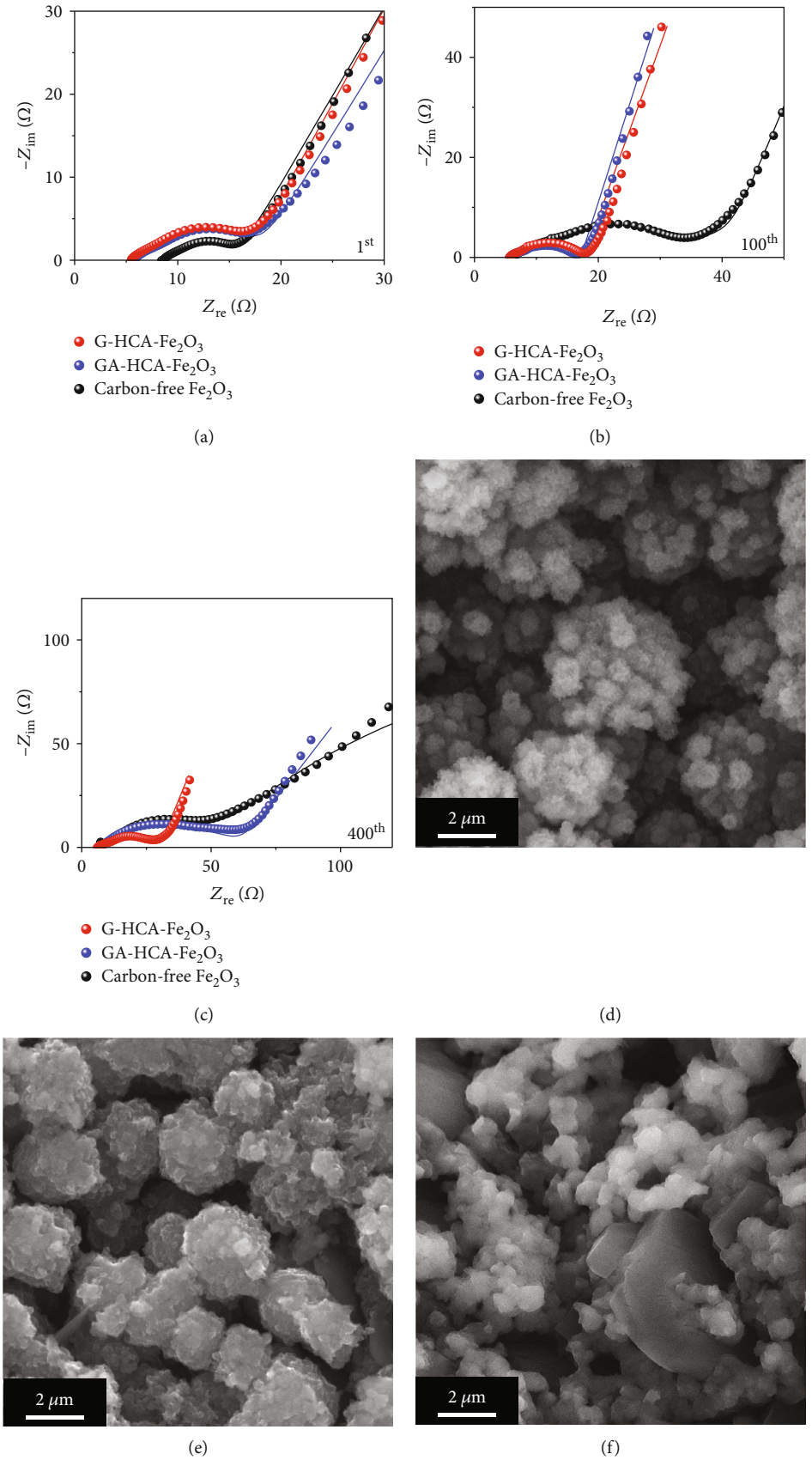

Figure 6: (a–c) Nyquist plots of G-HCA-Fe_2O_3, GA-HCA-Fe_2O_3, and carbon-free Fe_2O_3 microspheres obtained after the (a) 1st, (b) 100th, and (c) 400th cycles; SEM images of (d) G-HCA-Fe_2O_3, (e) GA-HCA-Fe_2O_3, and (f) carbon-free Fe_2O_3 microspheres after 400 cycles at 1 A g^{-1}.

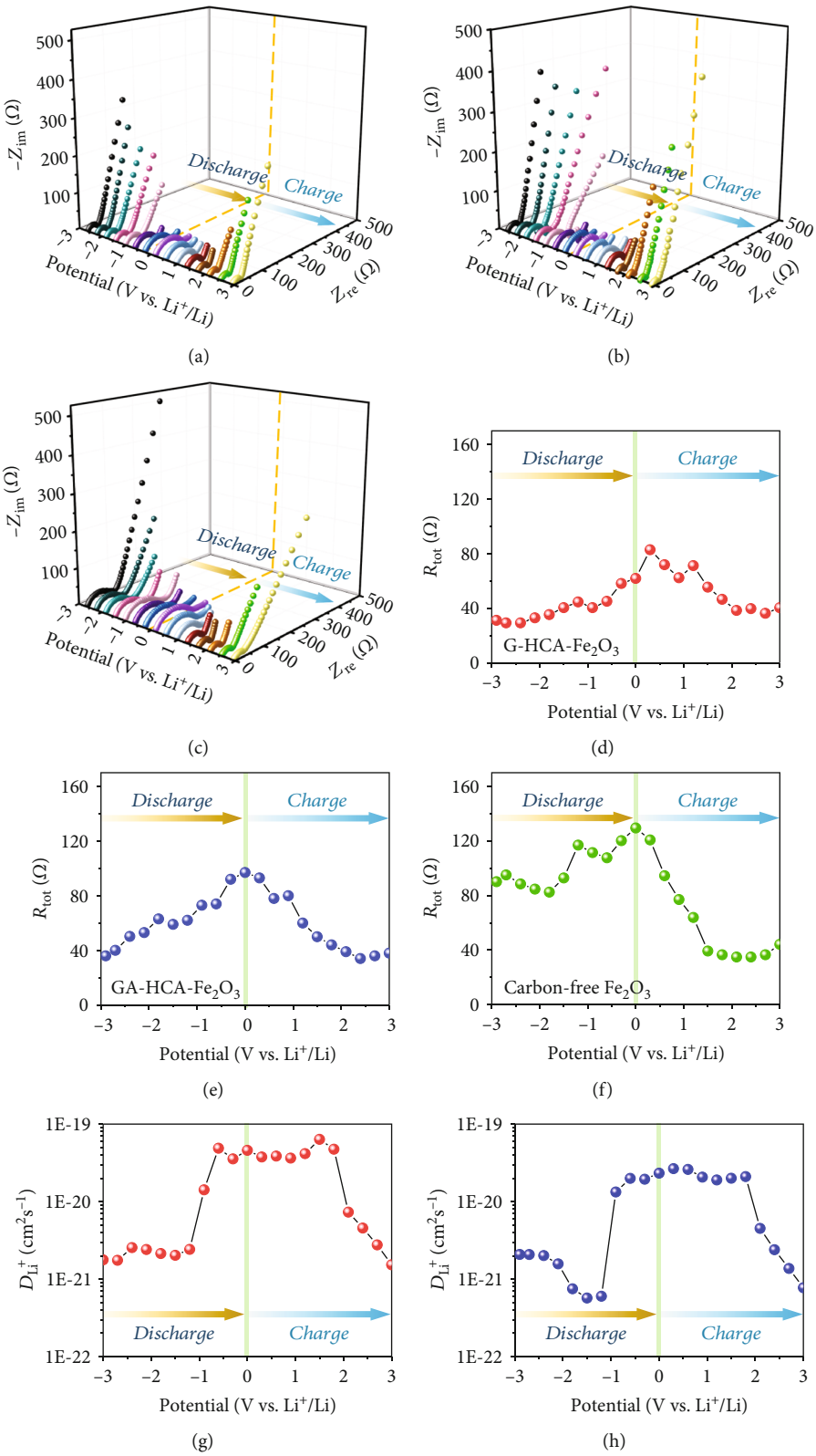

Figure 7: Continued.

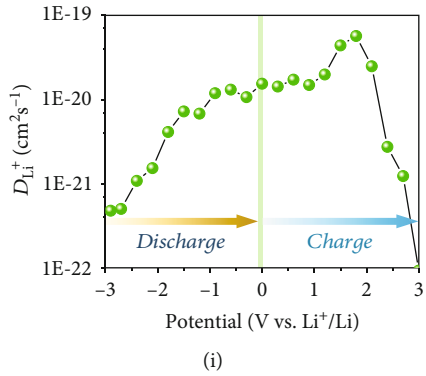

FIGURE 7: (a–c) In situ EIS Nyquist plots of the electrodes obtained at preselected potentials, (d–f) relationship between R_{tot} vs. potential and (g–i) D_{Li+} vs. potential for the initial discharge and charge processes corresponding to (a, d, and g) G-HCA-Fe_2O_3, (b, e, and h) GA-HCA-Fe_2O_3, and (c, f, and i) carbon-free Fe_2O_3 microspheres.

and bulky agglomeration occurred since the 3D porous carbon material was absent and the microsphere could not withstand the repetitive volume changes. The SEM images of a single microsphere after 400 cycles at 1 A g^{-1} revealed how the SEI layer is formed in each anode (Figure S25); the small particles that comprise G-HCA-Fe_2O_3 microspheres exhibited independent characteristics meaning that the thin SEI layer was formed on the surface (Figure S25a). GA-HCA-Fe_2O_3 microspheres maintained the original spherical shape; however, some agglomeration of the SEI layer could be observed on the surface of the microsphere (Figure S25b). In the case of carbon-free Fe_2O_3 microspheres, structural degradation occurred, and the SEI layer formed on the surface could be clearly discerned (Figure S25c).

To further elucidate the high electrochemical kinetics resulting in the structural robustness at high current densities, in situ EIS analysis was performed (Figure 7). The Nyquist plots of G-HCA-Fe_2O_3, GA-HCA-Fe_2O_3, and carbon-free Fe_2O_3 microspheres obtained during the charge–discharge process at 0.1 A g^{-1} are shown in Figures 7(a)–7(c). The negative and positive signs in Figure 7 indicate that the cell is in the discharge and charge states, respectively. Here, two depressed semicircles that appear in high- and medium-frequency regions, along with a linear component that appears at low-frequency region could be observed. From these, R_{tot}, which is referred to as the sum of R_{ct} and R_f, and diffusivity as a function of potential could be obtained and shown in Figures 7(d)–7(f) and Figures 7(g)–7(i), respectively [82]. R_{tot} values for all three samples exhibit increasing trends while being discharged to 0.001 V and decreasing trends upon charging to 3.0 V. The increase in R_{tot} upon discharging to −1.0 V may be attributed to the strain arising from volume changes during lithiation and phase transition from hexagonal α-$Li_xFe_2O_3$ to cubic $Li_2Fe_2O_3$ [67, 68]. Upon lithiation to −0.001 V, increase in R_{tot} values was observed even though there was a decrease in resistance due to the formation of Fe metal with high conductivity during conversion reaction at ~ −0.7 V [66, 67]. This effect is negated by the increase in R_{tot} owing to the formation of a highly resistive SEI film on the electrode surface. During the charging process, the R_{tot} values for all the samples gradually decrease as delithiation progresses, possibly because of the volume contraction and the decomposition of the highly resistive SEI layer. At potential higher than 2.0 V, R_{tot} values did not show much fluctuation since most of the SEI layer was decomposed. Notably, the R_{tot} values for carbon-containing Fe_2O_3 electrodes are considerably lower than those for carbon-free samples because the carbon framework provides the anodes with high electrical conductivity. The R_{tot} value for G-HCA-Fe_2O_3 microspheres is lower than that for GA-HCA-Fe_2O_3 owing to the highly graphitic nature of carbon in the 3D framework. Additionally, lithium-ion diffusion coefficients (D_{Li+}) can be calculated from the equation presented below (Equation (4)), whose parameters are described well in the previous studies [83]:

$$D_{Li+} = 0.5\left(\frac{RT}{sn^2F^2c\sigma}\right)^2. \quad (4)$$

D_{Li+} values of the three samples skyrocketed at potential near ~−0.7 V where conversion reaction that results in the formation of Fe metal with high electrical conductivity occurs, which indicates that the phases that comprise the electrode play a great role in diffusivity. Similarly, D_{Li+} values decline substantially after the conversion reaction that occurs at potential of approximately 2.0 V during the charge process. The D_{Li+} values for G-HCA-Fe_2O_3, GA-HCA-Fe_2O_3, and carbon-free Fe_2O_3 microspheres are between 1.5×10^{-21} and 6.3×10^{-20}, 5.7×10^{-22} and 2.6×10^{-20}, and 1.0×10^{-22} and 5.6×10^{-20}, respectively. The lithium-ion diffusion coefficients at different voltages are summarized in Table S4. G-HCA-Fe_2O_3 and GA-HCA-Fe_2O_3 microspheres exhibit higher D_{Li+} values than those for the carbon-free Fe_2O_3 microspheres at most potentials, which explains the high rate capability of those samples. Carbon-free Fe_2O_3 microspheres also showed good D_{Li+}, and some D_{Li+} values were comparable to the carbon-containing samples. This may be attributed to the highly porous nanostructure composed of small Fe_2O_3 nanoparticles, which contributes to good diffusivity. However, because

the structure is easily pulverized at high current densities (Figure S21) and the electrode is not composited with carbon with high electrical conductivity, the electrode exhibited low rate capability.

The difference in the D_{Li+} of G-HCA-Fe_2O_3, GA-HCA-Fe_2O_3, and carbon-free Fe_2O_3 microspheres was further validated by the Randles-Sevcik equation (Equation (5)), whose parameters are well described in the previous studies, to elucidate the origin of fast redox kinetics in G-HCA-Fe_2O_3 microspheres [84].

$$I_p = 0.4463nFAC\left(\frac{nFnD_{K^+}}{RT}\right)^{1/2} = \left[(269,000)n^{3/2}AD_{Li}{}^{+1/2}C\right]v^{1/2}. \quad (5)$$

The D_{Li+} values are calculated from the linear fitting of the data relevant to the peak current (I_p) and $v^{1/2}$ (Figure S26). In this study, A, n, and C, which correspond to the area of the electrode, number of electrons involved in the electrochemical reaction, and lithium-ion concentration, are 1.5 cm^2, 6, and 0.001 mol cm^{-3}, respectively. The D_{Li+} values for G-HCA-Fe_2O_3, GA-HCA-Fe_2O_3, and carbon-free Fe_2O_3 microspheres for the cathodic/anodic peaks are $1.26 \times 10^{-12}/4.01 \times 10^{-13}$, $8.36 \times 10^{-13}/3.31 \times 10^{-13}$, and $2.54 \times 10^{-13}/1.38 \times 10^{-13}$, respectively. The galvanostatic intermittent titration technique (GITT) was applied to further confirm that the rate capability of G-HCA-Fe_2O_3 microspheres was superior to those of GA-HCA-Fe_2O_3 and carbon-free Fe_2O_3 microspheres (Figure S27). The D_{Li+} values for the anode materials are calculated according to Fick's second law, the parameters of which have been described in previous reports [85].

$$D_{Li+} = \frac{4}{\pi\tau}\left(\frac{m_B V_M}{M_B S}\right)^2 \cdot \left(\frac{\Delta E_s}{\Delta E_\tau}\right)^2. \quad (6)$$

GITT analysis was performed at a current density of 0.1 A g^{-1} for 10 min followed by a relaxation time of 30 min (Figure S27a-c). During the initial discharge and charge processes, D_{Li+} values for G-HCA-Fe_2O_3 microspheres are higher than those for GA-HCA-Fe_2O_3 and carbon-free Fe_2O_3 microspheres at almost all potentials (Figure S27d,e). These results suggest that compositing transition metal oxides with carbon materials that exhibit higher electrical conductivity enhances the diffusion characteristics of lithium-ions. In addition, achieving a higher degree of graphitization in carbon materials led to an accelerated electrochemical kinetics.

4. Conclusion

In summary, a design strategy for the synthesis of 3D porous highly graphitic carbon microspheres to which numerous hollow metal oxide nanospheres are anchored and their application as anode for LIBs is reported. A facile spray drying process was used to generate 3D microspheres with numerous well-defined pores, which were subsequently infiltrated with iron salt using a drop-and-dry process. A series of heat treatment under Ar and ambient atmospheres formed highly graphitic carbon via the catalytic effect of metallic iron and the selective removal of amorphous carbon. Additionally, during the oxidation process, transformation of dense Fe into hollow Fe_2O_3 nanospheres simultaneously occurred owing to the nanoscale Kirkendall effect. Numerous hollow Fe_2O_3 nanospheres with reduced lithium-ion diffusion length were well-anchored on the inner surface of highly graphitic 3D porous carbon matrix, resulting in superb electrochemical properties, as evidenced by the ultrastable long-term cycle performance at high current density (10.0 A g^{-1}) and high rate capability (at 50.0 A g^{-1}). It is believed that the design strategy of anchoring hollow particles onto highly conductive 3D conductive carbon matrix can be tailored for use in various applications including energy storage, catalysts, and drug delivery.

Data Availability

Data is available on request.

Conflicts of Interest

The authors declare that they have no conflicts of interest.

Authors' Contributions

Soo Young Yang and Jin-Sung Park contributed equally to this work.

Acknowledgments

This research was supported by the National Research Council of Science & Technology (NST) grant by the Korea government (MSIT) (No. CAP22082-100). This research was supported by the National Research Foundation of Korea (NRF) grant funded by the Korea government (MSIT) (No. 2021M3H4A3A02086430).

Supplementary Materials

Additional supporting information may be found online in the Supporting Information at the end of the article. Supplementary Figure S1: (a,b) SEM images of SiO_2@RF nanoparticles-aggregated microspheres obtained from spray drying process. Supplementary Figure S2: (a,b) SEM image of SiO_2@C microspheres obtained from heat treatment of the spray-dried powder under Ar atmosphere. Supplementary Figure S3: (a) SEM and (d) TEM images of HCA microspheres. Supplementary Figure S4: morphologies of HCA microspheres prepared without dextrin, which is heat treated under Ar atmospheres: (a) before and (b) after NaOH etching. Supplementary Figure S5: (a,b) SEM images of HCA microspheres after iron nitrate infiltration. Supplementary Figure S6: XRD pattern of GA-HCA-Fe microspheres. Supplementary Figure S7: XRD pattern of HCA microspheres heat-treated under an Ar atmosphere. Supplementary Figure S8: morphological and structural characteristics of GA-HCA-Fe_2O_3 microspheres: (a) SEM, (b-d) TEM, and (e) HR-TEM images, (f) SAED pattern, and (g) elemental dot

mapping images. Supplementary Figure S9: (a) TEM image, (b) magnified TEM image, and (c-f) elemental mapping images of a broken G-HCA-Fe_2O_3 microsphere. Supplementary Figure S10: the overlapped elemental mapping images of G-HCA-Fe_2O_3 microspheres (Fe: orange, O: red, C: blue). Supplementary Figure S11: (a) SEM image and (b) XRD pattern of GA-HCA-Ni microspheres prepared from identical procedure. Supplementary Figure S12: morphological and structural characteristics of carbon-free Fe_2O_3 microspheres: (a) SEM, (b) TEM, and (c) HR-TEM images, (d) SAED pattern, and (e) elemental dot mapping images. Supplementary Figure S13: digital photographs of (a) carbon-free Fe_2O_3 and (b) G-HCA-Fe_2O_3 microspheres. Supplementary Figure S14: XPS spectra of (a,b) GA-HCA-Fe, (c,d) GA-HCA-Fe_2O_3, (e,f) G-HCA-Fe_2O_3, and (g,h) carbon-free Fe_2O_3 microspheres: (a,c,e,g) Fe 2p and (b,d,f,h) O 1 s spectra. Supplementary Figure S15: Randles-type equivalent circuit used to deconvolute the Nyquist plots. Supplementary Figure S16: BET analyses: (a) N_2 adsorption and desorption isotherms and (b) BJH pore size distribution of G-HCA-Fe_2O_3, GA-HCA-Fe_2O_3, and carbon-free Fe_2O_3 microspheres. Supplementary Figure S17: CV curves of (a) GA-HCA-Fe_2O_3 and (b) carbon-free Fe_2O_3 microspheres. Supplementary Figure S18: rate performances of GA-HCA-Fe_2O_3 and carbon-free Fe_2O_3 microspheres. Supplementary Figure S19: charge-discharge curves of (a) G-HCA-Fe_2O_3, (b) GA-HCA-Fe_2O_3, and (c) carbon-free Fe_2O_3 microspheres at various current densities. Supplementary Figure S20: retained capacity (%) vs. current density graphs of G-HCA-Fe_2O_3, GA-HCA-Fe_2O_3, and carbon-free Fe_2O_3 microspheres calculated from the rate capability test. The percentage of retained capacity was obtained with reference to the capacity at 0.5 A g^{-1}, which is considered as 100%. Supplementary Figure S21: cycle performances of GA-HCA-Fe_2O_3 and carbon-free Fe_2O_3 microspheres at 10.0 A g^{-1}. Supplementary Figure S22: SEM images revealing the thickness of G-HCA-Fe_2O_3 and carbon-free Fe_2O_3 microspheres before and after 100 cycles at 10 A g^{-1}. Supplementary Table S1: comparison of the electrochemical performances of various Fe_2O_3-based anode materials for LIB batteries. Supplementary Table S2: comparison of the electrochemical performances of various hollow metal oxide nanospheres and other materials with similar morphology for LIB batteries. Supplementary Figure S23: (a) cycle and (b) rate performances of G-HCA powder prepared from etching out Fe_2O_3 in G-HCA-Fe_2O_3 microspheres. Supplementary Figure S24: CV curves of (a) G-HCA-Fe_2O_3, (b) GA-HCA-Fe_2O_3, and (c) carbon-free Fe_2O_3 microspheres showing the surface-capacitive elements (in blue) and empirically obtained current (in grey) at a scan rate of 2.0 mV s^{-1}. Supplementary Table S3: various battery parameters obtained from the Nyquist plots using Zview software. Supplementary Figure S25: SEM images of (a) G-HCA-Fe_2O_3, (b) GA-HCA-Fe_2O_3, and (c) carbon-free Fe_2O_3 microspheres after 400 cycles at 1 A g^{-1}. Supplementary Table S4: lithium-ion diffusion coefficients of G-HCA-Fe_2O_3, GA-HCA-Fe_2O_3, and carbon-free Fe_2O_3 microspheres at different voltages (all numbers in the table are multiplied by 10^{-21}). Supplementary Figure S26: relationship between peak current (I_p) vs. square root of sweep rates ($v^{1/2}$) during (a-c) anodic and (d-f) cathodic sweep: graphs corresponding to (a,d) G-HCA-Fe_2O_3, (b,e) GA-HCA-Fe_2O_3, and (c,f) carbon-free Fe_2O_3 microspheres. Supplementary Figure S27: (a-c) GITT potential profiles of (a) G-HCA-Fe_2O_3, (b) GA-HCA-Fe_2O_3, and (c) carbon-free Fe_2O_3 microspheres, (d,e) Li-ion diffusion coefficient during (d) lithiation and (e) delithiation. *(Supplementary Materials)*

References

[1] B. Kang and G. Ceder, "Battery materials for ultrafast charging and discharging," *Nature*, vol. 458, no. 7235, pp. 190–193, 2009.

[2] Y. Liu, Y. Zhu, and Y. Cui, "Challenges and opportunities towards fast-charging battery materials," *Nature Energy*, vol. 4, no. 7, pp. 540–550, 2019.

[3] W. Dong, Y. Zhao, M. Cai et al., "Nanoscale borate coating network stabilized iron oxide anode for high-energy-density bipolar lithium-ion batteries," *Small*, vol. 19, no. 16, p. e2207074, 2023.

[4] M. Su, M. Li, K. He et al., "Structure and defect strategy towards high-performance copper niobate as anode for Li-ion batteries," *Chemical Engineering Journal*, vol. 455, p. 140802, 2023.

[5] S. Wang, L. Zhao, Y. Dong et al., "Pre-zeolite framework super-MIEC anodes for high-rate lithium-ion batteries," *Energy & Environmental Science*, vol. 16, no. 1, pp. 241–251, 2023.

[6] Y. Chen, B. Song, X. Tang, L. Lu, and J. Xue, "Ultrasmall Fe3O4nanoparticle/MoS2nanosheet composites with superior performances for lithium ion batteries," *Small*, vol. 10, no. 8, pp. 1536–1543, 2014.

[7] J. Wang, Z. Zhang, and H. Zhao, "SnS_2-SnS pn hetero-junction bonded on graphene with boosted charge transfer for lithium storage," *Nanoscale*, vol. 13, no. 48, pp. 20481–20487, 2021.

[8] Y. Chen, H. Xia, L. Lu, and J. Xue, "Synthesis of porous hollow Fe_3O_4 beads and their applications in lithium ion batteries," *Journal of Materials Chemistry*, vol. 22, no. 11, pp. 5006–5012, 2012.

[9] J. S. Park, J. S. Cho, J. H. Kim, Y. J. Choi, and Y. C. Kang, "Electrochemical properties of micron-sized Co_3O_4 hollow powders consisting of size controlled hollow nanospheres," *Journal of Alloys and Compounds*, vol. 689, pp. 554–563, 2016.

[10] Y. Lu, L. Yu, and X. W. Lou, "Nanostructured conversion-type anode materials for advanced lithium-ion batteries," *Chem*, vol. 4, no. 5, pp. 972–996, 2018.

[11] Y. X. Wang, J. Yang, S. L. Chou et al., "Uniform yolk-shell iron sulfide-carbon nanospheres for superior sodium-iron sulfide batteries," *Nature Communications*, vol. 6, no. 1, p. 8689, 2015.

[12] S. Li, A. Li, R. Zhang, Y. He, Y. Zhai, and L. Xu, "Hierarchical porous metal ferrite ball-in-ball hollow spheres: general synthesis, formation mechanism, and high performance as anode materials for Li-ion batteries," *Nano Research*, vol. 7, no. 8, pp. 1116–1127, 2014.

[13] R. Zhang, Y. He, and L. Xu, "Controllable synthesis of hierarchical $ZnSn(OH)_6$ and Zn_2SnO_4 hollow nanospheres and their applications as anodes for lithium ion batteries," *Journal of Materials Chemistry A*, vol. 2, no. 42, pp. 17979–17985, 2014.

[14] X. Wang, Y. Chen, Y. Fang, J. Zhang, S. Gao, and X. W. Lou, "Synthesis of cobalt sulfide multi-shelled nanoboxes with

precisely controlled two to five shells for sodium-ion batteries," *Angewandte Chemie, International Edition*, vol. 58, no. 9, pp. 2675–2679, 2019.

[15] Y. Huang, Z. Wang, M. Guan, F. Wu, and R. Chen, "Toward rapid-charging sodium-ion batteries using hybrid-phase molybdenum sulfide selenide-based anodes," *Advanced Materials*, vol. 32, no. 40, article e2003534, 2020.

[16] X. Zuo, Y. Wen, Y. Qiu et al., "Rational design and mechanical understanding of three-dimensional macro-/mesoporous silicon lithium-ion battery anodes with a tunable pore size and wall thickness," *ACS Applied Materials & Interfaces*, vol. 12, no. 39, pp. 43785–43797, 2020.

[17] B. Fei, Z. Yao, D. Cai et al., "Construction of sugar gourd-like yolk-shell Ni–Mo–Co–S nanocage arrays for high-performance alkaline battery," *Energy Storage Materials*, vol. 25, pp. 105–113, 2020.

[18] M. Chen, L. L. Shao, X. Q. Wang et al., "Controlled synthesis of highly active nonstoichiometric tin phosphide/carbon composites for electrocatalysis and electrochemical energy storage applications," *ACS Sustainable Chemistry & Engineering*, vol. 10, no. 4, pp. 1482–1498, 2022.

[19] M. Chen, Q. S. Jing, H. B. Sun et al., "Engineering the core–shell-structured NCNTs-Ni_2Si@porous Si composite with robust Ni–Si interfacial bonding for high-performance Li-ion batteries," *Langmuir*, vol. 35, no. 19, pp. 6321–6332, 2019.

[20] M. Chen, F. M. Liu, S. S. Chen, R. Wan, X. Qian, and Z. Y. Yuan, "Cactus-like iron oxide/carbon porous microspheres lodged in nitrogen-doped carbon nanotubes as anodic electrode materials of lithium ion batteries," *New Journal of Chemistry*, vol. 47, no. 2, pp. 765–771, 2023.

[21] M. Chen, F. M. Liu, H. Zhao et al., "In situ encapsulation of iron oxide nanoparticles into nitrogen-doped carbon nanotubes as anodic electrode materials of lithium ion batteries," *Physical Chemistry Chemical Physics*, vol. 24, no. 44, pp. 27114–27120, 2022.

[22] M. Chen, F. M. Liu, S. S. Chen et al., "In situ self-catalyzed formation of carbon nanotube wrapped and amorphous nanocarbon shell coated $LiFePO_4$ microclew for high-power lithium ion batteries," *Carbon*, vol. 203, pp. 661–670, 2023.

[23] M. Chen, F. M. Liu, S. S. Chen et al., "Low-temperature metal-catalyzed synthesis of encapsulated metal oxide nanoparticles in nitrogen-doped carbon nanotubes from carbon nitride as anodic materials of high-performance lithium-ion batteries," *New Journal of Chemistry*, vol. 47, no. 7, pp. 3215–3221, 2023.

[24] M. Chen, L. L. Shao, J. J. Li, W. J. Pei, M. K. Chen, and X. H. Xie, "One-step hydrothermal synthesis of hydrophilic Fe_3O_4/carbon composites and their application in removing toxic chemicals," *RSC Advances*, vol. 6, no. 42, pp. 35228–35238, 2016.

[25] T. Jiang, F. Bu, X. Feng, I. Shakir, G. Hao, and Y. Xu, "Porous Fe2O3nanoframeworks encapsulated within three-dimensional graphene as high-performance flexible anode for lithium-ion battery," *ACS Nano*, vol. 11, no. 5, pp. 5140–5147, 2017.

[26] J. S. Park, J. S. Cho, and Y. C. Kang, "Nickel vanadate microspheres with numerous nanocavities synthesized by spray drying process as an anode material for Li-ion batteries," *Journal of Alloys and Compounds*, vol. 780, pp. 326–333, 2019.

[27] Y. Yin, R. M. Rioux, C. K. Erdonmez, S. Hughes, G. A. Somorjal, and A. P. Alivisatos, "Formation of hollow nanocrystals through the nanoscale Kirkendall effect," *Science*, vol. 304, no. 5671, pp. 711–714, 2004.

[28] W. Wang, M. Dahl, and Y. Yin, "Hollow nanocrystals through the nanoscale Kirkendall effect," *Chemistry of Materials*, vol. 25, no. 8, pp. 1179–1189, 2013.

[29] J. S. Cho, S. Y. Lee, H. S. Ju, and Y. C. Kang, "Synthesis of NiO nanofibers composed of hollow nanospheres with controlled sizes by the nanoscale Kirkendall diffusion process and their electrochemical properties," *ACS Applied Materials & Interfaces*, vol. 7, no. 46, pp. 25641–25647, 2015.

[30] J. Sun, G. Zheng, H. W. Lee et al., "Formation of stable phosphorus-carbon bond for enhanced performance in black phosphorus nanoparticle-graphite composite battery anodes," *Nano Letters*, vol. 14, no. 8, pp. 4573–4580, 2014.

[31] X. W. Lou, D. Deng, J. Y. Lee, and L. A. Archer, "Preparation of SnO_2/carbon composite hollow spheres and their lithium storage properties," *Chemistry of Materials*, vol. 20, no. 20, pp. 6562–6566, 2008.

[32] S. Poyraz, "One-step preparation and characterization of a nanostructured hybrid electrode materialviaa microwave energy-based approach," *New Journal of Chemistry*, vol. 44, no. 25, pp. 10592–10603, 2020.

[33] Y. Liu, X. Zhang, S. Poyraz, C. Zhang, and J. H. Xin, "One-step synthesis of multifunctional zinc-iron-oxide hybrid carbon nanowires by chemical fusion for supercapacitors and interfacial water marbles," *ChemNanoMat*, vol. 4, no. 6, pp. 546–556, 2018.

[34] S. Poyraz, J. Cook, Z. Liu et al., "Microwave energy-based manufacturing of hollow carbon nanospheres decorated with carbon nanotubes or metal oxide nanowires," *Journal of Materials Science*, vol. 53, no. 17, pp. 12178–12189, 2018.

[35] J. Song, Y. Ji, Y. Li et al., "Porous carbon assisted carbon nanotubes supporting Fe_3O_4 nanoparticles for improved lithium storage," *Ceramics International*, vol. 47, no. 18, pp. 26092–26099, 2021.

[36] S. Gu and A. Zhu, "Graphene nanosheets loaded Fe_3O_4 nanoparticles as a promising anode material for lithium ion batteries," *Journal of Alloys and Compounds*, vol. 813, article 152160, 2020.

[37] Y. Chen, Z. Lu, L. Zhou, Y. W. Mai, and H. Huang, "In situ formation of hollow graphitic carbon nanospheres in electrospun amorphous carbon nanofibers for high-performance Li-based batteries," *Nanoscale*, vol. 4, no. 21, pp. 6800–6805, 2012.

[38] C. H. Jung, J. Choi, W. S. Kim, and S. H. Hong, "A nanopore-embedded graphitic carbon shell on silicon anode for high performance lithium ion batteries," *Journal of Materials Chemistry A*, vol. 6, no. 17, pp. 8013–8020, 2018.

[39] Q. Wang, W. Zhang, C. Guo, Y. Liu, C. Wang, and Z. Guo, "In situ construction of 3D interconnected FeS@Fe_3C@graphitic carbon networks for high-performance sodium-ion batteries," *Advanced Functional Materials*, vol. 27, no. 41, article 1703390, 2017.

[40] C. Wang, J. Yan, T. Li et al., "A coral-like FeP@NC anode with increasing cycle capacity for sodium-ion and lithium-ion batteries induced by particle refinement," *Angewandte Chemie, International Edition*, vol. 60, no. 47, pp. 25013–25019, 2021.

[41] Z. Huang, H. Hou, G. Zou et al., "3D porous carbon encapsulated SnO_2 nanocomposite for ultrastable sodium ion batteries," *Electrochimica Acta*, vol. 214, pp. 156–164, 2016.

[42] H. Jiang, Y. Zhang, L. Xu et al., "Fabrication of $(NH_4)_2V_3O_8$ nanoparticles encapsulated in amorphous carbon for high capacity electrodes in aqueous zinc ion batteries," *Chemical Engineering Journal*, vol. 382, article 122844, 2020.

[43] P. Lu, Y. Sun, H. Xiang, X. Liang, and Y. Yu, "3D amorphous carbon with controlled porous and disordered structures as a high-rate anode material for sodium-ion batteries," *Advanced Energy Materials*, vol. 8, no. 8, article 1702434, 2018.

[44] C. Liang, Y. Chen, M. Wu et al., "Green synthesis of graphite from CO_2 without graphitization process of amorphous carbon," *Nature Communications*, vol. 12, no. 1, p. 119, 2021.

[45] F. J. Maldonado-Hódar, C. Moreno-Castilla, J. Rivera-Utrilla, Y. Hanzawa, and Y. Yamada, "Catalytic graphitization of carbon aerogels by transition metals," *Langmuir*, vol. 16, no. 9, pp. 4367–4373, 2000.

[46] H. Zhang, O. Noonan, X. Huang et al., "Surfactant-free assembly of mesoporous carbon hollow spheres with large tunable pore sizes," *ACS Nano*, vol. 10, no. 4, pp. 4579–4586, 2016.

[47] A. Ōya and H. Marsh, "Phenomena of catalytic graphitization," *Journal of Materials Science*, vol. 17, no. 2, pp. 309–322, 1982.

[48] A. Gomez-Martin, Z. Schnepp, and J. Ramirez-Rico, "Structural evolution in iron-catalyzed graphitization of hard carbons," *Chemistry of Materials*, vol. 33, no. 9, pp. 3087–3097, 2021.

[49] P. W. Voorhees, "The theory of Ostwald ripening," *Journal of Statistical Physics*, vol. 38, no. 1-2, pp. 231–252, 1985.

[50] X. Yu, B. Qu, Y. Zhao et al., "Growth of hollow transition metal (Fe, Co, Ni) oxide nanoparticles on graphene sheets through Kirkendall effect as anodes for high-performance lithium-ion batteries," *Chemistry - A European Journal*, vol. 22, no. 5, pp. 1638–1645, 2016.

[51] U. N. Maiti, J. Lim, K. E. Lee, W. J. Lee, and S. O. Kim, "Three-dimensional shape engineered, interfacial gelation of reduced graphene oxide for high rate, large capacity supercapacitors," *Advanced Materials*, vol. 26, no. 4, pp. 615–619, 2014.

[52] S. T. Jackson and R. G. Nuzzo, "Determining hybridization differences for amorphous carbon from the XPS C 1s envelope," *Applied Surface Science*, vol. 90, no. 2, pp. 195–203, 1995.

[53] Y. J. Hong, K. C. Roh, and Y. C. Kang, "Superior lithium-ion storage performances of carbonaceous microspheres with high electrical conductivity and uniform distribution of Fe and TiO ultrafine nanocrystals for Li-S batteries," *Carbon*, vol. 126, pp. 394–403, 2018.

[54] Y. Zhong, L. Yu, Z. F. Chen et al., "Microwave-assisted synthesis of Fe3O4nanocrystals with predominantly exposed facets and their heterogeneous UVA/Fenton catalytic activity," *ACS Applied Materials & Interfaces*, vol. 9, no. 34, pp. 29203–29212, 2017.

[55] M. Mullet, V. Khare, and C. Ruby, "XPS study of Fe(II)-Fe(III) (oxy)hydroxycarbonate green rust compounds," *Surface and Interface Analysis*, vol. 40, no. 3-4, pp. 323–328, 2008.

[56] J. Wang, C. Gao, Z. Yang, M. Zhang, Z. Li, and H. Zhao, "Carbon-coated mesoporous silicon shell-encapsulated silicon nano-grains for high performance lithium-ion batteries anode," *Carbon*, vol. 192, pp. 277–284, 2022.

[57] R. Dong, L. Zheng, Y. Bai et al., "Elucidating the mechanism of fast Na storage kinetics in ether electrolytes for hard carbon anodes," *Advanced Materials*, vol. 33, no. 36, article 2008810, 2021.

[58] Z. Wang, H. Yang, Y. Liu et al., "Analysis of the stable interphase responsible for the excellent electrochemical performance of graphite electrodes in sodium-ion batteries," *Small*, vol. 16, no. 51, p. e2003268, 2020.

[59] S. Peng, X. Han, L. Li et al., "Unique cobalt sulfide/reduced graphene oxide composite as an anode for sodium-ion batteries with superior rate capability and long cycling stability," *Small*, vol. 12, no. 10, pp. 1359–1368, 2016.

[60] X. Yao, Y. Ke, W. Ren et al., "Defect-rich soft carbon porous nanosheets for fast and high-capacity sodium-ion storage," *Advanced Energy Materials*, vol. 9, no. 6, article 1803260, 2019.

[61] C. Chen, Y. Huang, C. An et al., "Copper-doped dual phase $Li_4Ti_5O_{12}$-TiO_2 nanosheets as high-rate and long cycle life anodes for high-power lithium-ion batteries," *ChemSusChem*, vol. 8, no. 1, pp. 114–122, 2015.

[62] K. Chen, H. N. Guo, W. Q. Li, and Y. J. Wang, "MOF-derived core-shell CoP@NC@TiO_2 Composite as a high-performance anode material for Li-ion batteries," *Chemistry – An Asian Journal*, vol. 16, no. 4, pp. 322–328, 2021.

[63] L. Ni, H. Chen, W. Deng et al., "Atomical reconstruction and cationic reordering for nickel-rich layered cathodes," *Advanced Energy Materials*, vol. 12, no. 11, article 2103757, 2022.

[64] Y. Zhang, H. Li, J. Liu, J. Liu, H. Ma, and F. Cheng, "Enhancing $LiNiO_2$ cathode materials by concentration-gradient yttrium modification for rechargeable lithium-ion batteries," *Journal of Energy Chemistry*, vol. 63, pp. 312–319, 2021.

[65] Z. Wang, X. Zhang, X. Liu, M. Lv, K. Yang, and J. Meng, "Co-gelation synthesis of porous graphitic carbons with high surface area and their applications," *Carbon*, vol. 49, no. 1, pp. 161–169, 2011.

[66] Z. Wang, D. Luan, S. Madhavi, Y. Hu, and X. W. Lou, "Assembling carbon-coated α-Fe2O3hollow nanohorns on the CNT backbone for superior lithium storage capability," *Energy & Environmental Science*, vol. 5, no. 1, pp. 5252–5256, 2012.

[67] D. Larcher, D. Bonnin, R. Cortes, I. Rivals, L. Personnaz, and J.-M. Tarascon, "Combined XRD, EXAFS, and Mössbauer studies of the reduction by lithium of $_{\alpha\text{-Fe[sub 2]O[sub 3]}}$ with various particle sizes," *Journal of the Electrochemical Society*, vol. 150, no. 12, pp. A1643–A1650, 2003.

[68] Y. Feng, N. Shu, J. Xie, F. Ke, Y. Zhu, and J. Zhu, "Carbon-coated Fe_2O_3 hollow sea urchin nanostructures as high-performance anode materials for lithium-ion battery," *Science China Materials*, vol. 64, no. 2, pp. 307–317, 2021.

[69] Q. Cheng and Y. Zhang, "Multi-channel graphite for high-rate lithium ion battery," *Journal of the Electrochemical Society*, vol. 165, no. 5, pp. A1104–A1109, 2018.

[70] C. Zhang, Z. Chen, H. Wang, Y. Nie, and J. Yan, "Porous Fe2O3nanoparticles as lithium-ion battery anode materials," *ACS Applied Nano Materials*, vol. 4, no. 9, pp. 8744–8752, 2021.

[71] T. Ishihara, A. Kawahara, H. Nishiguchi, M. Yoshio, and Y. Takita, "Effects of synthesis condition of graphitic nanocabon tube on anodic property of Li-ion rechargeable battery," *Journal of Power Sources*, vol. 97-98, pp. 129–132, 2001.

[72] R. Sun, S. Liu, Q. Wei et al., "Mesoporous NiS2nanospheres anode with pseudocapacitance for high-rate and long-life sodium-ion battery," *Small*, vol. 13, no. 39, article 1701744, 2017.

[73] S. Li, J. Qiu, C. Lai, M. Ling, H. Zhao, and S. Zhang, "Surface capacitive contributions: towards high rate anode materials for sodium ion batteries," *Nano Energy*, vol. 12, pp. 224–230, 2015.

[74] D. Su, K. Kretschmer, and G. Wang, "Improved electrochemical performance of Na-ion batteries in ether-based

electrolytes: a case study of ZnS nanospheres," *Advanced Energy Materials*, vol. 6, no. 2, p. 1501785, 2016.

[75] J. Liu, Y. Zhang, L. Zhang, F. Xie, A. Vasileff, and S. Z. Qiao, "Graphitic carbon nitride ($g\text{-}C_3N_4$)-derived N-rich graphene with tuneable interlayer distance as a high-rate anode for sodium-ion batteries," *Advanced Materials*, vol. 31, no. 24, article e1901261, 2019.

[76] S. Erol and M. E. Orazem, "The influence of anomalous diffusion on the impedance response of $LiCoO_2$|C batteries," *Journal of Power Sources*, vol. 293, pp. 57–64, 2015.

[77] U. Morali and S. Erol, "Analysis of electrochemical impedance spectroscopy response for commercial lithium-ion batteries: modeling of equivalent circuit elements," *Turkish Journal of Chemistry*, vol. 44, no. 3, pp. 602–613, 2020.

[78] S. Erol, "Process model development of lithium-ion batteries—an electrochemical impedance spectroscopy simulation," *Sakarya University Journal of Science*, vol. 24, no. 6, pp. 1191–1197, 2020.

[79] S. Erol, "A statistical design approach on electrochemical impedance spectroscopy of NMC Li-ion battery," *Journal of the Electrochemical Society*, vol. 169, no. 10, article 100503, 2022.

[80] U. Moralı and S. Erol, "Electrochemical impedance analysis of 18650 lithium-ion and 6HR61 nickel-metal hydride rechargeable batteries," *Journal of the Faculty of Engineering and Architecture of Gazi University*, vol. 35, pp. 297–309, 2020.

[81] S. Erol, *Impedance Analysis and Modeling of Lithium-Ion Batteries*, LAMBERT Academic Publishing, Saarbrucken, Germany, 2016.

[82] J. Liu, Q. Duan, M. Ma, C. Zhao, J. Sun, and Q. Wang, "Aging mechanisms and thermal stability of aged commercial 18650 lithium ion battery induced by slight overcharging cycling," *Journal of Power Sources*, vol. 445, article 227263, 2020.

[83] Y. Sun, J. Tang, K. Zhang et al., "Comparison of reduction products from graphite oxide and graphene oxide for anode applications in lithium-ion batteries and sodium-ion batteries," *Nanoscale*, vol. 9, no. 7, pp. 2585–2595, 2017.

[84] H. G. Jung, J. Hassoun, J. B. Park, Y. K. Sun, and B. Scrosati, "An improved high-performance lithium-air battery," *Nature Chemistry*, vol. 4, no. 7, pp. 579–585, 2012.

[85] H. Zhang, P. Zong, M. Chen et al., "In situ synthesis of multilayer carbon matrix decorated with copper particles: enhancing the performance of Si as anode for Li-ion batteries," *ACS Nano*, vol. 13, no. 3, pp. 3054–3062, 2019.